3. Results

3.1 Relationship between average intensity of pixels and incoming light intensity

The obtained relationship between average intensities of pixels and relative incoming light intensities controlled by ND filters is shown in Fig. 6. The solid line represents the regression line obtained by the least squares method. The correlation coefficient was above 0.99. This result indicates that the calculated average intensity of pixels and the light intensity entering the object lens are in proportion.

3.2 Time dependence of fluorescence decay

To examine the time dependence of fluorescence decay[15] of the object cells, GFP intensity was measured every one second in the same frame ($n = 10$). Normalized GFP intensity, which was obtained from GFP intensity at each second divided by the initial GFP intensity, was plotted against exposure time to excitation light (Fig. 7). The result shown in Fig. 7 indicates that GFP intensity decreases to 30% of the initial GFP intensity with 20-second exposure to excitation light. As exposure to excitation light reduces fluorescence intensity, to obtain sharp photographs, the time interval between the start of exposure to excitation light and the capture of images should be shortened. In this study, this time interval was 1–2 seconds because it takes that long to set the optical path and capture an image.

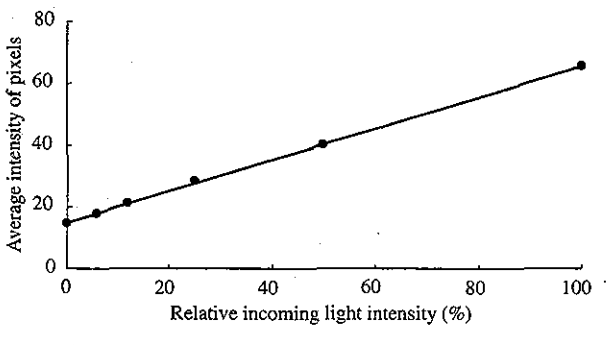

Fig. 6 Average intensities of pixels versus relative incoming light intensities. The solid line shows a linear fit to the data points using the least squares method. The correlation coefficient is above 0.99. This result indicates that the average intensity of pixels is proportional to the intensity of the incoming light.

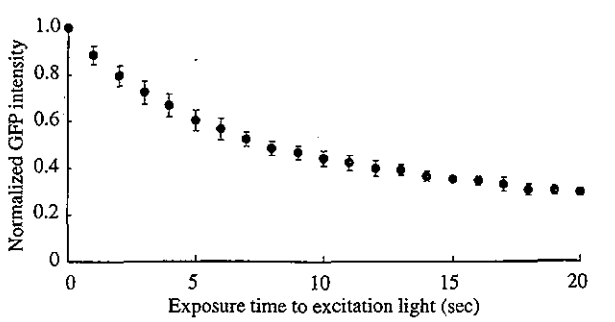

Fig. 7 Time course of fluorescence decay of hrGFP. GFP intensity was measured every one second and normalized by the initial GFP intensity ($n = 10$). GFP intensity was decreased to 30% of the initial GFP intensity by 20-second exposure to excitation light. Error bars show ±SD.

3.3 GFP intensity and charge density of prestin-expressing CHO cells

Representative data of the hrGFP fluorescence image, a brightness histogram of the pixels included within the outline of the target cell and measured membrane capacitance against membrane potential of the target cell are shown in Fig. 8.

In a group of 20 cells, fitting parameters of $C_{\mathrm{lin}} = 18.6 \pm 5.5$ pF, $Q_{\max} = 126.2 \pm 107.2$ fC, $\alpha = 41.3 \pm 10.7$ mV and $V_{1/2} = -57.9 \pm 13.2$ mV, and charge density of $394 \pm 227\ e^-/\mu m^2$ were obtained from patch-clamp recordings (mean ± SD).

The obtained charge density was plotted against GFP intensity (Fig. 9). The regression line was calculated using the least squares method. The correlation coefficient obtained from least squares fit is 0.67. This correlation between charge density and GFP intensity is significant at the 0.05 level.

4. Discussion

The fitting parameters α and $V_{1/2}$ of Eq. (2), which reflect the characteristic properties of prestin, obtained from 20 cells, correspond well with findings of previous reports[10],[16], supporting the validity of the measurements. The average value of charge density, i.e., 394 $e^-/\mu m^2$, obtained from 20 cells, is larger than that previously reported, i.e., 196 $e^-/\mu m^2$[12]. In this study, cells showing bright fluorescence were selected, while the previous study, cells were chosen at random. It is therefore considered that the charge density of 394 $e^-/\mu m^2$ obtained in this study is not indicative of the average charge density of the whole group of prestin-expressing CHO cells.

Membrane capacitance of cells, which did not fluoresce, was also measured. However, those cells did not show voltage dependent nonlinear capacitance. These results indicate that prestin was not expressed or was only slightly expressed in the cells which did not fluoresce. These results agree with the fact that there is a correlation between GFP intensity and the expression level of prestin.

As shown in Fig. 9, it was clarified that there was a correlation between the GFP intensity and the expression level of prestin although the correlation coefficient was 0.67. This result indicates that the expression level of prestin can be estimated by using GFP intensity. The cells which show high GFP intensity should be selected when high prestin-expressing cells are required.

To obtain GFP intensity with less error, the time interval between the start of exposure to excitation light and

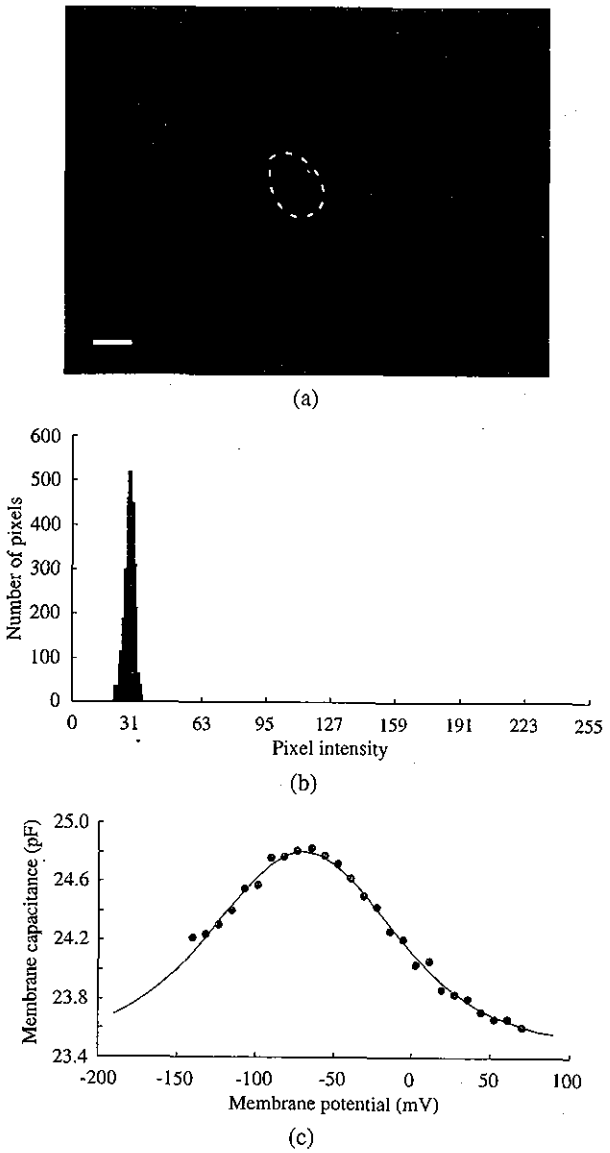

Fig. 8 Representative data of a prestin-expressing CHO cell. (a) hrGFP fluorescence image of a cell. The dashed circular curve is the outline of the target cell. Scale bar is 10 μm. (b) Brightness histogram of the target area. GFP intensity of the cell was determined to be 27.8. (c) Membrane capacitance versus membrane potential of the cell shown in (a). Data points were fitted with Eq. (2), which is shown by the solid line, with the following parameters: $C_{lin} = 23.4$ pF, $Q_{max} = 220.5$ fC, $\alpha = 40.7$ mV and $V_{1/2} = -71.7$ mV. Charge density of 589 $e^-/\mu m^2$ was obtained from these fitting parameters.

the capture of images should be the same because GFP intensity is reduced with time due to fluorescence decay (Fig. 7). In this study, however, the time interval between the start of exposure to excitation light and the capture of images ranged from one to two seconds. According to Fig. 7, there is a possibility that the obtained GFP intensity has a margin of error of up to 20%. Another way to reduce error is to apply a weaker excitation light and to improve

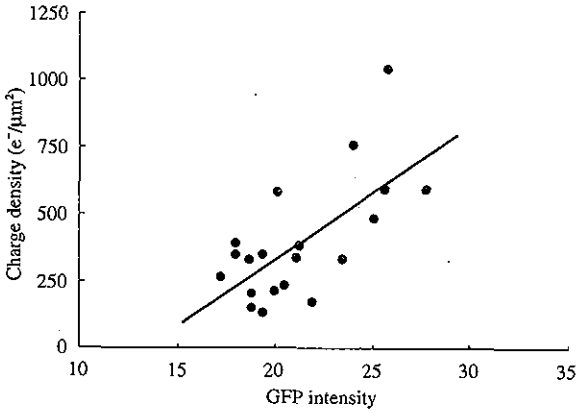

Fig. 9 Relationship between charge density and GFP intensity of prestin-expressing CHO cells. The solid line shows a linear fit to the data points using the least squares method. The correlation coefficient is 0.67. This relationship is significant at the 0.05 level. $n = 20$

the detection sensitivity of fluorescence because the application of weaker excitation light restricts the fluorescence decay.

5. Conclusions

It was demonstrated that hrGFP fluorescence intensity increases linearly as charge density increases. As charge density is proportional to the expression level of prestin, this result indicates that such expression can be evaluated by relative hrGFP fluorescence intensity in the constructed cell line.

Acknowledgements

This work was supported by a grant from the Human Frontier Science Program, by a Health and Labour Science Research Grant from the Ministry of Health, Labour and Welfare of Japan, and by Grant-in-Aid for Scientific Research on Priority Areas 15086202 from the Ministry of Education, Culture, Sports, Science and Technology of Japan.

References

(1) Davis, H., An Active Process in Cochlear Mechanics, Hear. Res., Vol.9 (1983), pp.79–90.
(2) Brownell, W.E., Bader, D. and Ribaupierre, Y., Evoked Mechanical Responses of Isolated Cochlear Outer Hair Cells, Science, Vol.227 (1985), pp.194–196.
(3) Dallos, P. and Evans, B.N., High-Frequency Motility of Outer Hair Cells and the Cochlear Amplifier, Science, Vol.267 (1995), pp.2006–2009.
(4) Kachar, B., Brownell, W.E., Altschuler, R. and Fex, J., Electrokinetic Shape Changes of Cochlear Outer Hair Cells, Nature, Vol.322 (1986), pp.365–368.
(5) Kalinec, F., Holley, M.C., Iwasa, K.H., Lim, D.J. and Kachar, B., A Membrane-Based Force Generation Mechanism in Auditory Sensory Cells, Proc. Natl. Acad. Sci. USA, Vol.86 (1992), pp.8671–8675.

(6) Santos-Sacchi, J. and Dilger, J.P., Whole Cell Currents and Mechanical Responses of Isolated Outer Hair Cells, Hear. Res., Vol.35 (1988), pp.143–150.
(7) Zenner, H.P., Motile Responses in Outer Hair Cells, Hear. Res., Vol.22 (1986), pp.83–90.
(8) Ashmore, J.F., A Fast Motile Response in Guinea-Pig Outer Hair Cells: The Cellular Basis of the Cochlear Amplifier, J. Physiol., Vol.388 (1987), pp.323–347.
(9) Zheng, J., Shen, W., He, D.Z.Z., Long, K.B., Madison, L.D. and Dallos, P., Prestin Is the Motor Protein of Cochlear Outer Hair Cells, Nature, Vol.405 (2000), pp.149–155.
(10) Ludwig, J., Oliver, D., Frank, G., Klöcker, N., Gummer, A.W. and Fakler, B., Reciprocal Electromechanical Properties of Rat Prestin: The Motor Molecule from Rat Outer Hair Cells, Proc. Natl. Acad. Sci. USA, Vol.98 (2001), pp.4178–4183.
(11) Liberman, M.C., Gao, J., He, D.Z.Z., Wu, X., Jia, S. and Zuo, J., Prestin Is Required for Electromotility of the Outer Hair Cell and for the Cochlear Amplifier, Nature, Vol.419 (2002), pp.300–304.
(12) Iida, K., Konno, K., Oshima, T., Tsumoto, K., Ikeda, K., Kumagai, I., Kobayashi, T. and Wada, H., Stable Expression of the Motor Protein Prestin in Chinese Hamster Ovary Cells, JSME Int. J., Ser. C, Vol.46, No.4 (2003), pp.1266–1274.
(13) Chalfie, M., Tu, Y., Euskirchen, G., Ward, W.W. and Prasher, D.C., Green Fluorescent Protein as a Marker for Gene Expression, Science, Vol.263 (1994), pp.802–805.
(14) Neher, E. and Marty, A., Discrete Changes of Cell Membrane Capacitance Observed under Conditions of Enhanced Secretion in Bovine Adrenal Chromaffin Cells, Proc. Natl. Acad. Sci. USA, Vol.79 (1982), pp.6712–6716.
(15) Swaminathan, R., Hoang, C.P. and Verkman, A.S., Photobleaching Recovery and Anisotropy Decay of Green Fluorescent Protein GFP-S65T in Solution and Cells: Cytoplasmic Viscosity Probed by Green Fluorescent Protein Translational and Rotational Diffusion, Biophys. J., Vol.72 (1997), pp.1900–1907.
(16) Oliver, D., He, D.Z.Z., Klöcker, N., Ludwig, J., Schulte, U., Waldegger, S., Ruppersberg, J.P., Dallos, P. and Bernd, F., Intracellular Anions as the Voltage Sensor of Prestin, the Outer Hair Cell Motor Protein, Science, Vol.292 (2001), pp.2340–2343.

Prediction of the characteristics of two types of pressure waves in the cochlea: Theoretical considerations

Masayoshi Andoh and Hiroshi Wada[a)]
Department of Bioengineering and Robotics, Tohoku University, Sendai 980-8579, Japan

(Received 25 June 2003; revised 19 April 2004; accepted 26 April 2004)

The aim of this study was to predict the characteristics of two types of cochlear pressure waves, so-called fast and slow waves. A two-dimensional finite-element model of the organ of Corti (OC), including fluid–structure interaction with the surrounding lymph fluid, was constructed. The geometry of the OC at the basal turn was determined from morphological measurements of others in the gerbil hemicochlea. As far as mechanical properties of the materials within the OC are concerned, previously determined mechanical properties of portions within the OC were adopted, and unknown mechanical features were determined from the published measurements of static stiffness. Time advance of the fluid–structure scheme was achieved by a staggered approach. Using the model, the magnitude and phase of the fast and slow waves were predicted so as to fit the numerically obtained pressure distribution in the scala tympani with what is known about intracochlear pressure measurement. When the predicted pressure waves were applied to the model, the numerical result of the velocity of the basilar membrane showed good agreement with the experimentally obtained velocity of the basilar membrane documented by others. Thus, the predicted pressure waves appeared to be reliable. Moreover, it was found that the fluid–structure interaction considerably influences the dynamic behavior of the OC at frequencies near the characteristic frequency. © *2004 Acoustical Society of America.* [DOI: 10.1121/1.1763599]

PACS numbers: 43.64.Bt, 43.64.Kc [BLM] Pages: 417–425

I. INTRODUCTION

When a fluid pressure fluctuation is induced by vibration of the stapes, two types of pressure waves occur in the cochlea. Lighthill (1981) theoretically characterized these pressure waves. One is a fast wave which is a compressional wave caused by the stapes vibration. It is uniformly distributed over the cross-section of each scala, i.e., the scala vestibuli (SV), the scala media (SM) and the scala tympani (ST), respectively, and propagates at the velocity of sound. As each scala is divided by Reissner's membrane or the basilar membrane (BM), the magnitude and/or phase difference of the fast wave between the scalae is possibly caused by the stiffness and damping of the membrane. The other is a slow wave which results from a fluid flow according to the interaction between the BM and the lymph fluid, i.e., it follows a traveling wave on the BM. The slow wave exists in the vicinity of the BM and has equal magnitude with opposite phases at either side of the BM (Lighthill, 1981). Olson (1999) found a notch in the frequency response of the intracochlear pressure, and explained that this notch was caused by the destructive interaction between two modes of pressure waves. As the organ of Corti (OC) is driven by these pressure waves, it is important to understand their frequency characteristics. However, there have been no reports on empirical observations of these waves, because of the difficulty of measuring them independently. Therefore, numerical analysis would seem to be useful for clarifying their frequency characteristics.

As the OC is immersed in lymph fluid, the interaction between the OC and the lymph fluid must be taken into account when the dynamic behavior of the OC and fluid pressure distribution are numerically analyzed. However, the complex structure of the OC and the large difference in material properties between the fluid and the structure of the OC complicate modeling of the lymph–OC interaction. Prior attempts to construct a cochlear model including the microstructure within the OC (Kolston and Ashmore, 1996) have been inconclusive, because only the lymph fluid in the SV was considered.

In the present study, finite-element models of the OC and the lymph fluid surrounding the OC are constructed to predict the frequency characteristics of the two types of pressure waves. The fluid–structure interaction between the model of the OC and those of the lymph fluid is considered by means of a staggered approach. Using these models, first, unknown Young's moduli of individual portions within the OC model are determined based on the static stiffness measurement of the OC (Naidu and Mountain, 1998). The frequency characteristics of the fast and slow waves are then predicted so as to fit the numerically obtained distribution of the intracochlear pressure with the experimentally obtained one (Olson, 2001).

II. MODEL

A. Geometry

The amplitude of the BM vibration in the gerbil cochlea is approximately 5 nm when a pure tone of 80 dB SPL is applied to the ear canal (Ren, 2002). Due to this tiny vibration amplitude and the longitudinally extending structure of the OC, it is assumed that the cross section of the OC main-

a)Electronic mail: wada@cc.mech.tohoku.ac.jp

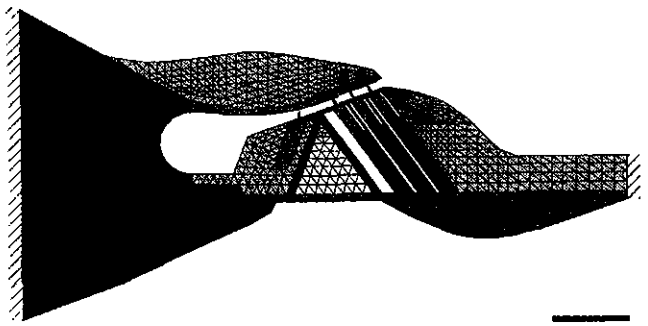

FIG. 1. Model of the organ of Corti discretized with finite elements. The number of nodes is 1274 and the number of elements is 2139. Each shade of gray in the model indicates the portion which has the same mechanical property. Scale bar represents 50 μm.

tains its plane surface when external force is applied. The two-dimensional OC model was therefore constructed under the plane strain condition. The OC at the basal turn of the gerbil cochlea, located 2.5–3.0 mm from the base, is modeled as shown in Fig. 1. The characteristic frequency (CF) of the OC at this location is approximately 16 kHz. Right and left boundaries of the OC model were fixed. Table I indicates geometric parameters of the OC model which are determined based on measurement in the hemicochlea of the gerbil (Edge *et al.*, 1998). Meshing is done at a subcellular level using a triangular element, by which the number of nodes and elements are 1274 and 2139, respectively. The fluid within the Corti tunnel is treated as an elastic body without shear stiffness. Although there is no element in the sub-tectorial space, the viscous force is considered analytically on the assumption that Couette flow occurs in this space. The effect of the mass of the fluid in the sub-tectorial space is assumed to be negligible, because the volume of this space is inconsiderable in comparison with that of the SV.

To simulate the behavior of the lymph fluid and its interaction with the OC, models of the lymph fluid in the SV and the ST are constructed as shown in Figs. 2(a) and (b), respectively. As Reissner's membrane is extremely compliant, it is considered to have little influence on the dynamic behavior of the lymph fluid. Reissner's membrane was, therefore, omitted and the SM was considered to be a part of the SV. The dark area of each model corresponds to the OC. As the lymph fluid in the scalae is assumed to move not only in the radial and transversal directions but also in the longitudinal direction, three-dimensional fluid models were, therefore, constructed. The dynamic behavior of the local section of the OC, which extends in the longitudinal direction, was

TABLE I. Geometric parameters of the OC model. BM, TM, IPC, OPC, and RL are abbreviations for basilar membrane, tectorial membrane, inner pillar cell, outer pillar cell, and reticular lamina, respectively. RL/BM angle indicates an angle between the RL and BM (after Edge *et al.*, 1998).

BM width	170 μm
BM maximum thickness	35 μm
TM width	130 μm
TM maximum thickness	40 μm
OPC height	70 μm
IPC height	55 μm
RL/BM angle	20°

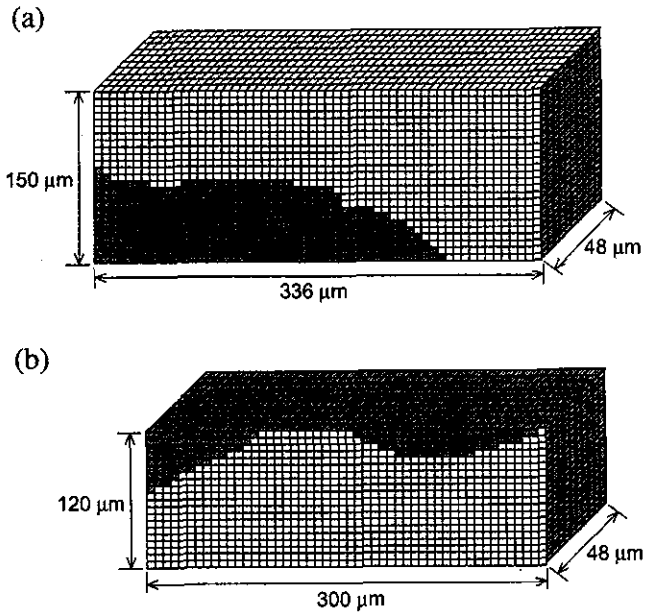

FIG. 2. Models of the lymph fluid. (a) Scala vestibuli. (b) Scala tympani. Dark area in each model corresponds to the OC.

simulated in this study, and thus longitudinal widths of both fluid models were determined to be 48 μm, which is less than one-fourth of the wavelength of the traveling wave (Ren, 2002). In consideration of the modiolus and the cochlear wall, the left and right boundaries of these models are fixed. The boundary of the SV model at 150 μm from the BM and that of the ST model at 120 μm from the BM are also fixed because it is assumed that the lymph fluid does not move across those boundaries. A grid with intervals of 6 μm makes it possible to evaluate the pressure distribution around the OC in the scalae. As a result, the SV model and the ST model have 11 200 and 8000 cubic elements, respectively.

B. Mechanical properties

Young's moduli of individual portions in the model are based on measurements *in vitro* and *in situ*. Young's modulus assigned to the model is 3.0×10^4 N/m^2 at the tectorial membrane (TM) (Steele *et al.*, 2000), 1.0×10^4 N/m^2 at the outer hair cells (OHCs) (Ulfendahl and Chen, 1998), 1.0×10^7 N/m^2 at the phalanxes (Laffon and Angelini, 1996), and 1.0×10^9 N/m^2 at the pillar cells (Tolomeo and Holley, 1997). Young's moduli of the inner hair cell (IHC) and Deiters' cells are assumed to be the same as those of the OHCs and the phalanxes, respectively. Young's moduli of Kimura's membrane and the reticular lamina (RL) are assumed to be 1.0×10^6 N/m^2 and 1.0×10^9 N/m^2, respectively, because these structures would be stiff enough to support adjacent structures. Young's modulus for the osseous spiral lamina is assumed to be 2×10^{10} N/m^3, which is the same value as that of the cortical bone (Ashman *et al.*, 1984), because both of them are composed of bony material. Young's modulus of the stereocilia and its stiffness relative to the tip displacement are assumed to be 1.0×10^7 N/m^2 (Zetes and Steele, 1997) and 2.5×10^{-3} N/m (Langer *et al.*, 2001), respectively.

Although Young's moduli of the BM and Hensen's cell would have a profound effect on the dynamic behavior of the

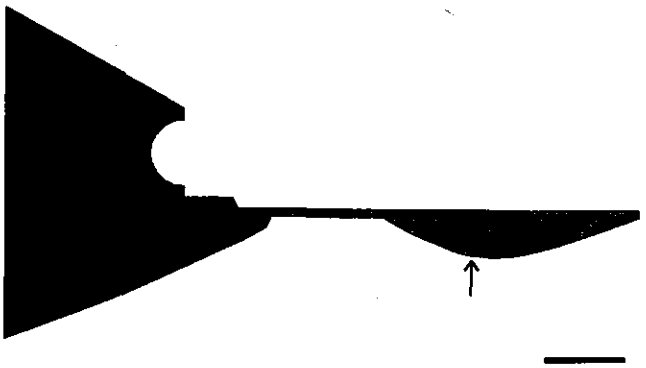

FIG. 3. Model of the BM. This model is a reduced representation of the OC model shown in Fig. 1. Using this model, the stiffness of the BM is calculated to determine the Young's modulus of the BM. The arrow indicates the point where the force is applied and the stiffness is evaluated.

OC, those of the gerbil have not been reported. To determine Young's moduli of these portions, the stiffness of the OC obtained by numerical analysis is compared with that of the gerbil measured by Naidu and Mountain (1998). According to their experiment, the stiffness of the OC is 2–4 N/m at a point beneath the OHCs when the OC at the basal turn is statically deflected. If the cells are removed from the BM, the stiffness of the BM is assumed to be 1.3–2.6 N/m at a point beneath the OHCs. Using the BM model shown in Fig. 3, which is a reduced representation of the OC model, Young's modulus of the BM is determined to be 1.0×10^7 N/m^2. Using the OC model shown in Fig. 1, Young's modulus of Hensen's cells is then determined to be 5.0×10^3 N/m^2.

The Poisson's ratio of soft cells and the TM, which is composed of an extracellular matrix, is assumed to be 0.49 because these portions are nearly incompressible, whereas those of hard cells and the osseous spiral lamina are assumed to be 0.3 because this value is commonly used in structure analysis.

To guide the eye, the OC model shown in Fig. 1 is colored with shades of gray, a different shade being used for each portion having the same mechanical properties. For the lymph fluid models shown in Figs. 2(a) and (b), mechanical properties are assumed to be the same as those of water. Table II shows all mechanical properties of the models.

TABLE II. Mechanical properties assigned to the OC and fluid models.

	Young's modulus (N/m^2)	Poisson's ratio
BM	1.0×10^7	0.3
Deiters' cell	1.0×10^7	0.3
Hensen's cell	5.0×10^3	0.49
Inner hair cell	1.0×10^4	0.49
Kimura's membrane	1.0×10^6	0.3
Osseous spiral lamina	2.0×10^{10}	0.3
OHC	1.0×10^4	0.49
Phalanx	1.0×10^7	0.3
Pillar cell	1.0×10^9	0.3
RL	1.0×10^9	0.3
Stereocilia	1.0×10^7	0.3
TM	3.0×10^4	0.49

The density and viscosity of the lymph fluid are 1.0×10^3 kg/m^3 and 1.0×10^{-3} Pa·s, respectively, which are equal to those of water.

C. Formulation

In the OC model, it is assumed that the cross section of the OC maintains its plane surface when external force is applied to the OC. Therefore, the model of the OC is formulated under the plane strain condition. The equation of the motion of the structure by the finite-element process is represented by the following matrix differential equation:

$$[\mathrm{M}]\frac{\partial^2\mathbf{u}_s}{\partial t^2}+[\mathrm{C}]\frac{\partial\mathbf{u}_s}{\partial t}+[\mathrm{K}]\mathbf{u}_s=\mathbf{f}, \tag{1}$$

where [M], [C], and [K] are the mass, damping, and stiffness matrices, respectively, $\mathbf{u}_s$ is the structural displacement vector, $\mathbf{f}$ is the force vector, and t is the time. The damping matrix [C] is derived from the linear combination of mass and stiffness matrices, i.e.,

$$[\mathrm{C}]=\alpha[\mathrm{M}]+\beta[\mathrm{K}], \tag{2}$$

where α and β are Rayleigh damping parameters. In the Newmark-β method (Newmark, 1959), the displacement vector at the end of a time interval can be expressed in terms of the displacement, velocity and acceleration vectors at the beginning of the interval as follows:

$$\left([\mathrm{K}]+\frac{2}{\delta t}[\mathrm{C}]+\frac{4}{(\delta t)^2}[\mathrm{M}]\right)\mathbf{u}_s^{n+1}$$
$$=\mathbf{f}^{n+1}+[\mathrm{M}]\left(\frac{\partial^2\mathbf{u}_s^n}{\partial t^2}+\frac{4}{\delta t}\frac{\partial\mathbf{u}_s^n}{\partial t}+\frac{4}{(\delta t)^2}\mathbf{u}_s^n\right)$$
$$+[\mathrm{C}]\left(\frac{\partial\mathbf{u}_s^n}{\partial t}+\frac{2}{\delta t}\mathbf{u}_s^n\right), \tag{3}$$

where δt is the time interval and n is the time step. The velocity and acceleration vectors at the end of a time interval can be expressed in terms of the velocity and acceleration vectors at the beginning of the time interval and the displacement vector at the end of the time interval by the relations

$$\frac{\partial\mathbf{u}_s^{n+1}}{\partial t}=-\frac{\partial\mathbf{u}_s^n}{\partial t}+\frac{2}{\delta t}(\mathbf{u}_s^{n+1}-\mathbf{u}_s^n), \tag{4}$$

$$\frac{\partial^2\mathbf{u}_s^{n+1}}{\partial t^2}=-\frac{\partial^2\mathbf{u}_s^n}{\partial t^2}-\frac{4}{\delta t}\frac{\partial\mathbf{u}_s^n}{\partial t}+\frac{4}{(\delta t)^2}(\mathbf{u}_s^{n+1}-\mathbf{u}_s^n). \tag{5}$$

Using Eqs. (3)–(5), values of the vectors at time step $n+1$ can be obtained from the previously determined values of the vectors and the known value of the force vector.

Regarding the lymph fluid, the Reynolds number (Re) of fluid flow is defined as

$$\mathrm{Re}=\frac{\rho\mathrm{UL}}{\mu}, \tag{6}$$

where U is the approximate maximum fluid velocity in the vicinity of the BM, L is the length of the BM, ρ is the density of water (1×10^3 kg/m^3), and μ is the viscosity of water (1×10^{-3} Pa·s). As characteristic values are U=1 mm/s estimated from experimental data (Olson, 2001) and L=170 μm, Re becomes 0.17. In this range of Reynolds number, an incompressible and viscous flow can be assumed, and thus

an incompressible Navier–Stokes equation is used to analyze the dynamic behavior of the lymph fluid. The incompressible Navier–Stokes equation is as follows:

$$\frac{\partial \mathbf{v}_f}{\partial t}+(\mathbf{v}_f\cdot\nabla)\mathbf{v}_f+\frac{1}{\rho}\nabla p_{OC}-\upsilon\Delta\mathbf{v}_f=0, \tag{7}$$

where $\mathbf{v}_f$ is the fluid velocity vector, p_{OC} is the fluid pressure caused by the OC motion, υ is the kinetic viscosity of the fluid, t is the time, and the gradient operator ∇ and the Laplacian operator Δ are defined in the following form

$$\nabla=\left(\frac{\partial}{\partial x},\frac{\partial}{\partial y},\frac{\partial}{\partial z}\right),\quad \Delta=\frac{\partial^2}{\partial x^2}+\frac{\partial^2}{\partial y^2}+\frac{\partial^2}{\partial z^2}. \tag{8}$$

Using a Marker-and-Cell (MAC) method (Harlow and Welch, 1965), the fluid is decomposed into rectangular parallelepiped cells and the pressure is discretized at the center of the cell. Discretizing the diffusion term and convection term explicitly and the pressure term implicitly in Eq. (7), the discrete Navier–Stokes equation is derived as follows:

$$\frac{\mathbf{v}_f^{n+1}-\mathbf{v}_f^n}{\delta t}+(\mathbf{v}_f^n\cdot\nabla)\mathbf{v}_f^n+\frac{1}{\rho}\nabla p_{OC}^{n+1}-\upsilon\Delta\mathbf{v}_f^n=0, \tag{9}$$

where δt is the time interval and n is the time step. Rewriting Eq. (9) leads to

$$\mathbf{v}_f^{n+1}=\mathbf{v}_f^n-\delta t\left\{(\mathbf{v}_f^n\cdot\nabla)\mathbf{v}_f^n+\frac{1}{\rho}\nabla p_{OC}^{n+1}-\upsilon\Delta\mathbf{v}_f^n\right\}. \tag{10}$$

Considering the divergence of Eq. (10) leads to

$$\nabla\cdot\mathbf{v}_f^{n+1}=\nabla\cdot\mathbf{v}_f^n-\delta t\nabla\cdot\left\{(\mathbf{v}_f^n\cdot\nabla)\mathbf{v}_f^n+\frac{1}{\rho}\nabla p_{OC}^{n+1}-\upsilon\Delta\mathbf{v}_f^n\right\}. \tag{11}$$

Following the continuity equation of fluid, $\nabla\cdot\mathbf{v}_f^{n+1}=0$. By contrast, to reduce numerical error, the first term of the right side $\nabla\cdot\mathbf{v}_f^n$ is allowed to remain. As a consequence, Eq. (11) becomes

$$\Delta p_{OC}^{n+1}=\rho\left[\frac{1}{\delta t}\nabla\cdot\mathbf{v}_f^n-\nabla\cdot\{(\mathbf{v}_f^n\cdot\nabla)\mathbf{v}_f^n-\upsilon\Delta\mathbf{v}_f^n\}\right]. \tag{12}$$

Substituting the known value of fluid velocity vector $\mathbf{v}_f^n$ into Eq. (12), p_{OC}^{n+1} can be obtained, and then $\mathbf{v}_f^{n+1}$ is obtainable from Eq. (10).

In this study, as a structural model (OC) and a fluid model (lymph fluid) are constructed separately, the fluid–structure interaction between the model of the OC and that of the lymph fluid is considered by applying a staggered approach. As shown in Fig. 4, the procedure for coupling the fluid and structure equations is as follows: In time step $n=1$, by multiplying the initial pressure p_{INT}^1, which is a summation of the fast and slow waves, with the area of the fluid–structure (F-S) interface of the OC model, the force vector $\mathbf{f}^1$ over the F-S interface of the OC model is obtained. Applying the force vector $\mathbf{f}^1$ to Eq. (3), the displacement vector $\mathbf{u}_s^1$ can be obtained, and then substituting it into Eq. (4), the velocity vector $\partial\mathbf{u}_s^1/\partial t$ is obtainable. Assuming $\partial\mathbf{u}_s^1/\partial t=\mathbf{v}_f^0$ at the F-S interface, the fluid pressure p_{OC}^1 caused by the OC motion is

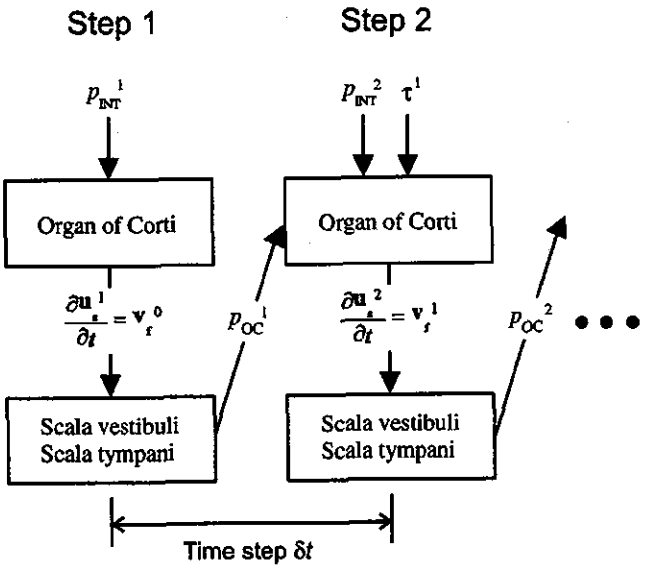

FIG. 4. Scheme of the fluid–structure interaction using the staggered approach. In time Step 1, initial pressure p_{INT}^1 caused by the fast and slow waves is applied to the equations of the OC [Eqs. (3) and (4)] and the velocity of the OC $\partial\mathbf{u}_s^1/\partial t$ is obtained. Then, applying this velocity $\partial\mathbf{u}_s^1/\partial t$ to the equation of the lymph fluid [Eq. (12)] as a fluid velocity $\mathbf{v}_f^0$ over a fluid–structure interface, the fluid pressure p_{OC}^1 in each scala caused by the movement of the OC is obtained at the same time step. In Step 2, this obtained fluid pressure p_{OC}^1, the initial pressure p_{INT}^2 in time Step 2 and shear stress τ^1 exerted on the TM and RL are applied to the equation of the OC. By repeating the above procedure, the time history of the movement of the OC and that of the pressure distribution in each scala are obtained.

obtainable by Eq. (12). In time step $n=2$, assuming Couette flow in the sub-tectorial space, the shear stress vector $\boldsymbol{\tau}^1$ exerted on the TM and the RL is given by

$$\boldsymbol{\tau}^1=\mu\frac{\mathbf{v}_{RELATIVE}^1}{2h}, \tag{13}$$

where $\mathbf{v}_{RELATIVE}^1$ is the relative velocity vector between the TM and RL, h is the clearance between the TM and the RL. Multiplying the shear stress vector $\boldsymbol{\tau}^1$ in the sub-tectorial space by areas of the TM and RL, and multiplying the previously obtained fluid pressure p_{OC}^1 and the initial pressure p_{INT}^2 in time step $n=2$ by the area of the F-S interface, the force vector $\mathbf{f}^2$ in time step $n=2$ is obtained. This obtained force vector $\mathbf{f}^2$ is applied to Eq. (3). By repeating the above procedure, the time history of the movement of the OC and that of the pressure distribution in each scala are obtained. In this study, the passive cochlea is assumed. Therefore, the force generated by the OHC motility is not taken into account. As mentioned in the Introduction, when numerical calculations are carried out, it is assumed that the fast wave is uniform over the cross-sections of both scalae, and the slow wave is applied to the F-S interface of the OC model and has equal magnitude with opposite phases at either side of the BM.

Numerical calculations are performed on a COMPAQ DS-20E using a 64-bit floating point number representation. Calculation is executed for four cycles for each sinusoidal frequency and took 2 hours.

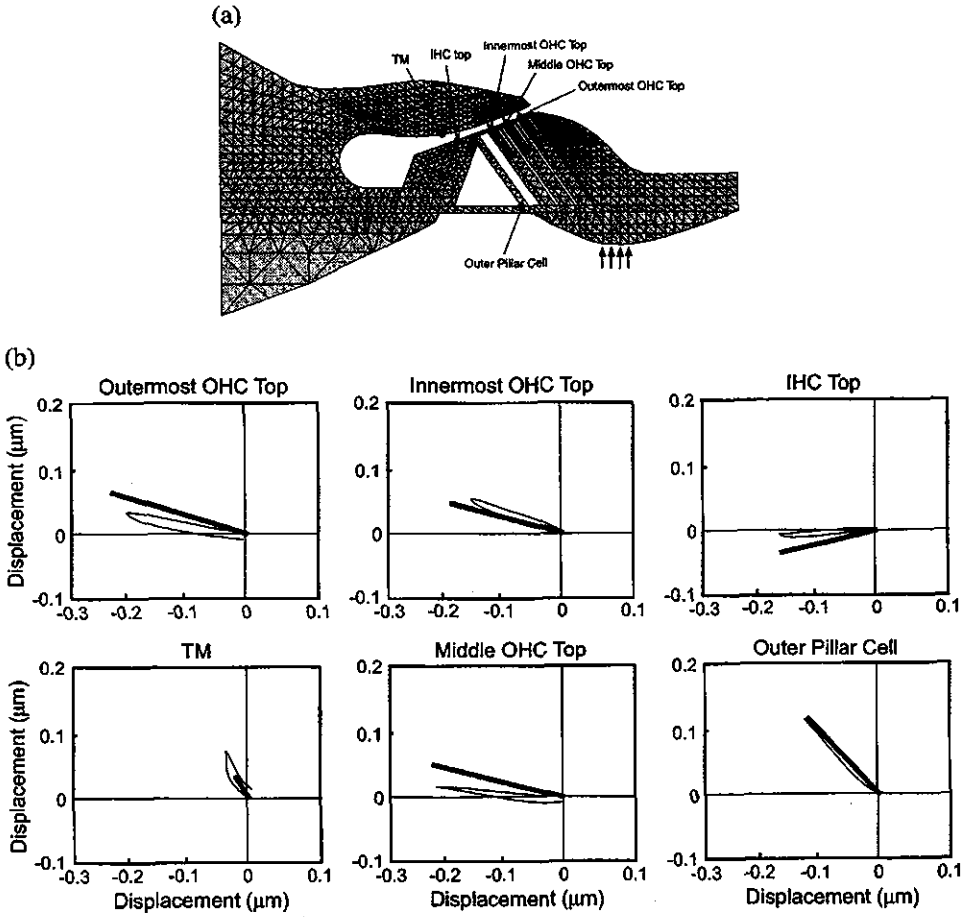

FIG. 5. Trajectories of cochlear structures. (a) Points of measurement when a sinusoidal force of 2.0 Hz and 1.0×10^{-6} N is applied to the bottom of the BM (arrows), such force being similar to the experiment using the hemicochlea. (b) Trajectories of each point within the OC. The horizontal axis is parallel to the BM, and the vertical axis is perpendicular to the BM. Thin lines are the experimental results (Hu *et al.*, 1999) and thick lines are the numerical results.

III. VALIDATION OF THE MODEL: STATIC DISPLACEMENT

When a sinusoidal force of 2.0 Hz and 1.0×10^{-6} N is applied to the bottom of the BM, the amplitude and angle of the each point within the OC model is calculated. This stimulation is equivalent to that of the hemicochlea experiment (Hu *et al.*, 1999), i.e., the application of oscillatory force via a glass paddle. Experimentally obtained trajectories of each measurement point [points in Fig. 5(a)] and those of numerical results are shown by thin and thick lines in Fig. 5(b), respectively.

A comparison between numerical and experimental results reveals that the numerically obtained amplitude and angle at the innermost OHC and outer pillar cell are nearly the same as those obtained by the experiment. However, angles of the outermost OHC top, middle OHC top, and IHC top differ from the experimental values by 7.5° at the outermost OHC top, 10.2° at the middle OHC top, and 11.1° at the IHC top. These discrepancies would result because the angle between the RL and the BM of the model is different from that in the hemicochlea. From the above-mentioned comparison, it is confirmed that the mechanical properties of the model are appropriate.

IV. PREDICTION OF THE CHARACTERISTICS OF THE FAST AND SLOW WAVES

The procedure for predicting the frequency characteristics of the fast and slow waves, which are initial pressures applied to the OC model, is as follows: First, the frequency characteristics of the fast wave in the SV ($P_{fast\text{-}SV}$) are estimated by an analytical method. Second, taking account of the experimentally obtained fluid pressure in the ST (Olson, 2001), the frequency characteristics of the fast wave in the

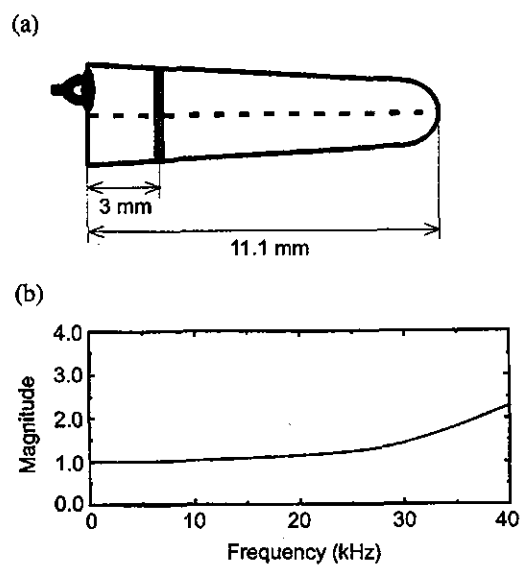

FIG. 6. Frequency response of the fast wave at 3 mm from the base in the gerbil cochlea. (a) Schema of the cochlea and the site where the model is constructed. The total length of the gerbil cochlea is 11.1 mm and the OC at 3 mm from the base (shaded area) is modeled. (b) Magnitude of the fast wave as a function of frequency which is derived from Eq. (14). Magnitude is relative to the sound pressure at the base.

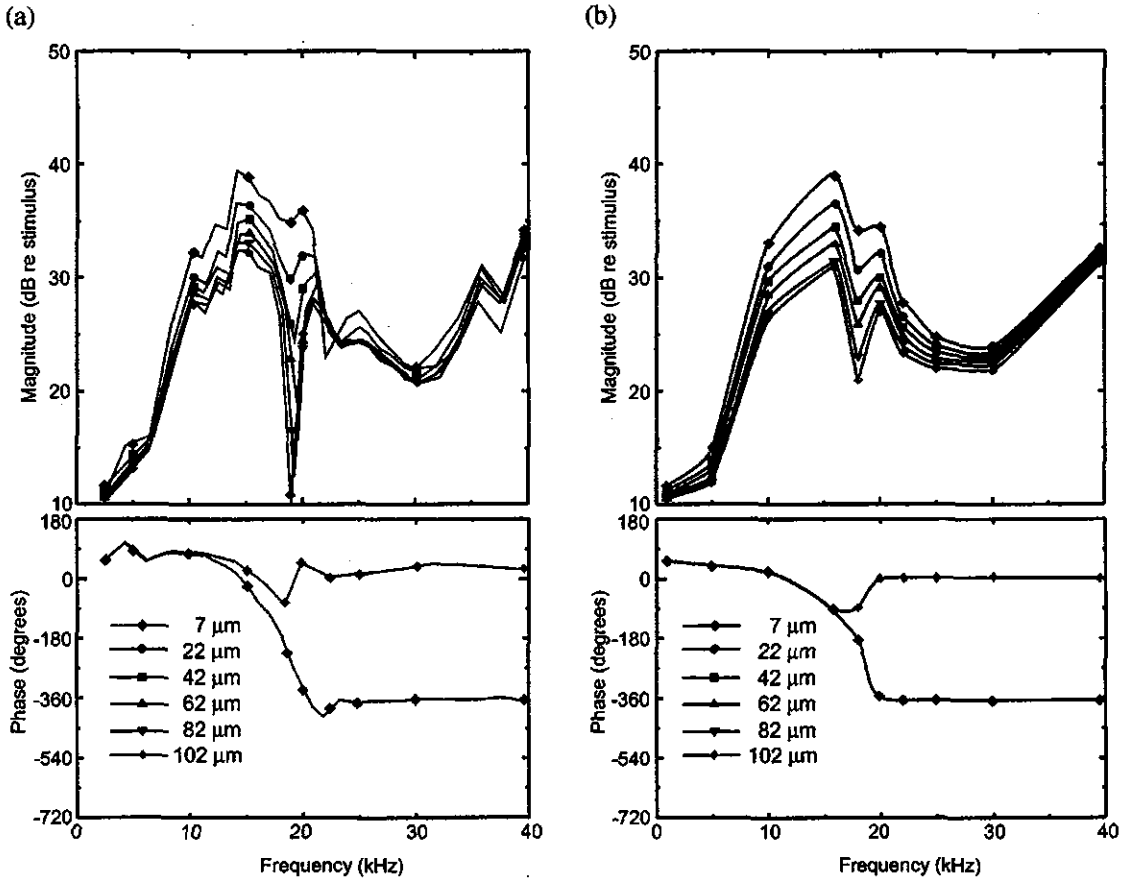

FIG. 7. Magnitude and phase of the fluid pressure in the ST versus frequency when a pure tone of 80 dB SPL is applied to the ear canal. The key indicates the distance from the BM. (a) Experimental data from the basal turn where the CF is about 16 kHz [Olson's Figs. 7(c) and (d) 2001]. (b) Numerical results. Magnitude is relative to the stimulus level in the ear canal. Phase is relative to the pressure near the stapes.

ST ($P_{fast\text{-}ST}$) are estimated. Finally, by comparing these experimental data with the numerical results, the frequency characteristics of the slow wave (P_{slow}) are estimated.

When it is assumed that the cochlea is a tapered closed tube, i.e., the cross-sectional area of the cochlea becomes smaller towards the apex, the magnitude of the fast wave $f(x)$ can be described as follows (Lighthill, 1981):

$$f(x)=f(0)\{J_0[\omega c_0^{-1}(L-x)]\}/\{J_0(\omega c_0^{-1}L)\}, \qquad (14)$$

where $f(0)$ is the magnitude of the fast wave at the base, L is a length of the cochlea, x is the distance from the base, J_0 is the first zero of the Bessel function, ω is the angular frequency, and c_0 is the velocity of sound in water. In this study, the length of the cochlea L is set to be 11.1 mm (Müller, 1996). Figure 6(a) is a schema of the gerbil cochlea indicating the location for which the model is constructed, and Fig. 6(b) shows the magnitude of $f(x)$ relative to $f(0)$ as a function of frequency in the gerbil cochlea at $x=3$ mm. The magnitude of the fast wave increases with increasing frequency and quarter-wavelength resonance occurs at 48 kHz. The frequency characteristics of $P_{fast\text{-}SV}$ are estimated as follows:

(1) The fluid pressure in the vicinity of the stapes is estimated to be 105 dB SPL when the sound stimulus of 80 dB SPL is applied to the ear canal due to the gain of 25 dB in the middle ear. Therefore, it is estimated that the magnitude of $P_{fast\text{-}SV}$ is 105 dB SPL at 1 kHz and increases gradually with increasing frequency and reaches 112 dB SPL at 40 kHz in accordance with Eq. (14).

(2) The phase difference of $P_{fast\text{-}SV}$ relative to the pressure near the stapes is zero for the entire frequency range because the footplate of the stapes is connected to the basal end of the SV and a fast wave propagates at the velocity of sound.

Figure 7(a) shows the experimental data on the fluid pressure in the ST in the basal turn of the gerbil cochlea when a pure tone of 80 dB SPL is applied to the ear canal (Olson, 2001). In that experiment, advancing and retracting the pressure sensor to and from the BM while keeping it perpendicular to the BM, the fluid pressures in the ST were measured at intervals of approximately 20 μm. The base point of the distance from the BM was determined by touching the BM with the sensor. The post-mortem data were changed very little from the pre-mortem one at 80 dB SPL in that experiment, so the pre-mortem data are comparable to our numerical results obtained from the model in which the force generated by the OHC motility is not included. Taking these experimental data into account, the frequency characteristics of $P_{fast\text{-}ST}$ are estimated as follows and as shown in Fig. 7(b):

(3) In the experimental data, the difference of the magnitude of the fluid pressure between nearest-neighbor mea-

suring points for a certain frequency becomes small with increasing distance from the BM, except for frequencies close to the CF of 16 kHz. Because P_{slow} exists in the vicinity of the BM in contrast to $P_{fast\text{-}ST}$ which is uniform in the ST, this behavior implies that the magnitude of P_{slow} does not have a significant effect on the pressure at points far from the BM, i.e., $P_{fast\text{-}ST}$ is dominant. Therefore, from the experimental data at 120 μm from the BM, it is estimated that the magnitude of $P_{fast\text{-}ST}$ is 90 dB SPL at 1 kHz, 93 dB SPL at 5 kHz, 102 dB SPL at 30 kHz, and 111 dB SPL at 40 kHz. The magnitudes of $P_{fast\text{-}ST}$ between 5 and 30 kHz are estimated using linear interpolation.

(4) The phase difference of $P_{fast\text{-}ST}$ relative to the pressure near the stapes is estimated based on the experimental data at 102 μm from the BM, i.e., 60° below 10 kHz and 0° above 16 kHz. This phase advance below 10 kHz can be explained as being due to the damping of the OC (Olson, 2001). The OC is between the SV and ST, and the damping of the OC causes the phase advance of $P_{fast\text{-}ST}$ relative to $P_{fast\text{-}SV}$.

On the other hand, as P_{slow} is regarded as being fluid pressure propagation caused by the fluid flux in the vicinity of the BM, the frequency responses of P_{slow} are similar to those of the traveling wave on the BM. It is widely accepted that the magnitude of the traveling wave increases with increasing frequency up to the CF, and then decays sharply. Therefore, the frequency characteristics of P_{slow} are assumed to be as follows:

(5) The phase delay of the traveling wave is assumed to originate at 1 kHz. And then, following the experimentally obtained phase difference of the fluid pressure at 7 μm from the BM, where P_{slow} is dominant, it is estimated that the phase difference of P_{slow} is $-180°$ at 18 kHz, resulting in destructive interference with $P_{fast\text{-}ST}$ which is observed as a pressure notch in the experimental data. Above 25 kHz, the phase of P_{slow} cannot be estimated because the fast wave dominates the pressure distribution in the cochlea, so that it is considered to be a constant $-360°$ according to the experimental data. Therefore, the phase differences of P_{slow} over the entire frequency range are estimated as shown in Fig. 8(b) using cubic interpolation.

(6) Applying the magnitude and phase of $P_{fast\text{-}SV}$ and $P_{fast\text{-}ST}$ and the phase of P_{slow} to the model, the magnitude of P_{slow} is estimated so as to fit the pressure distribution in the ST obtained by our numerical analysis with that of the experimental data. The stapes vibration at the base of the cochlea generates $P_{fast\text{-}SV}$. At the same time, the BM is vibrated by the stapes vibration via lymph fluid, resulting in a traveling wave on the BM, i.e., P_{slow}. Therefore, the magnitudes of $P_{fast\text{-}SV}$ and P_{slow} are assumed to be the same at the base (Lighthill, 1981). The magnitude of the traveling wave is known to increase as a function of frequency till the stimulus frequency reaches the CF; however, its increase is quite small well below the CF (Ren and Nuttall, 2001). Therefore, at 1 kHz, it is assumed that the magnitude of P_{slow} at 3 mm from the base is the same as that at the base, because 1 kHz is substantially small relative to the CF (16 kHz). $P_{fast\text{-}SV}$ is nearly the same over the entire length of the cochlea except around the quarter-wavelength resonance (48 kHz). As a consequence, at 1 kHz and 3 mm from the base where the model is constructed, it is assumed that the magnitude of P_{slow} has the same value as that of $P_{fast\text{-}SV}$. The magnitude of P_{slow} gradually increases with increasing frequency and reaches a maximum of 125 dB SPL at the CF. The magnitude of P_{slow} is followed by 122 dB SPL at 18 kHz and 110 dB SPL at 22 kHz. Above 25 kHz, the magnitude of P_{slow} is calculated to be 70 dB SPL, a limit beyond which the pressure in the ST at 7 μm from the BM changes more than 1 dB.

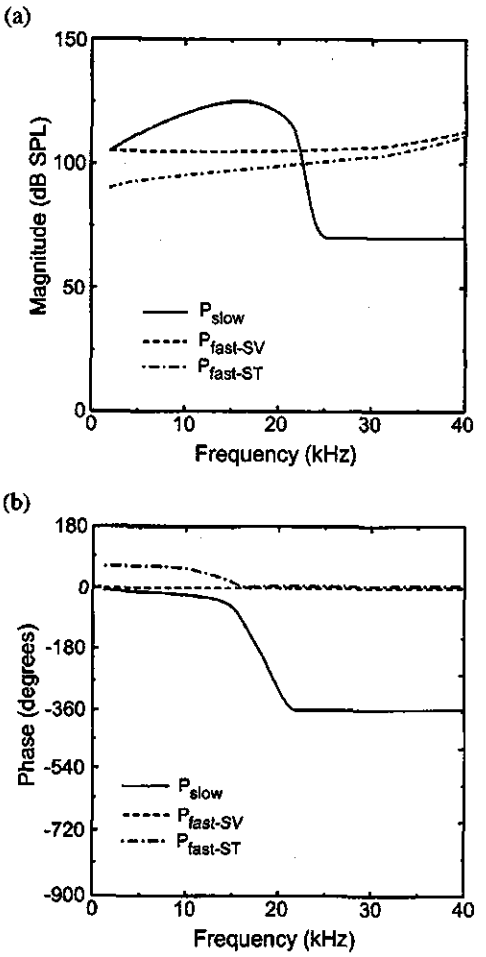

FIG. 8. Numerically obtained frequency characteristics of the slow wave, the fast waves in the SV and the ST when the magnitude and phase of the fluid pressure in the ST are shown in Fig. 7(b). The slow wave is applied to the F-S interface of the OC model and the fast waves are applied to the fluid models uniformly. (a) Magnitude. (b) Phase. Above 25 kHz, the magnitude of P_{slow} is calculated to be 70 dB SPL, a limit beyond which the pressure in the ST at 7 μm from the BM changes more than 1 dB, and the phase of P_{slow} is considered to be a constant $-360°$.

Figure 7(b) shows the numerically obtained pressure distribution in the ST when these predicted pressure waves, which are shown in Figs. 8(a) and (b), are applied to the model. The pressure peak at 16 kHz, the pressure notch at 18 kHz, the pressure increase from 30 kHz, and the phase of pressure relative to the pressure near the stapes are consistent with those of the experimental data. However, the depth and sharpness of the pressure notch at 18 kHz are different. The reason for this discrepancy might be the difference between the boundary condition in the model of the ST and the actual situation in the real cochlea at 120 μm from the BM. Con-

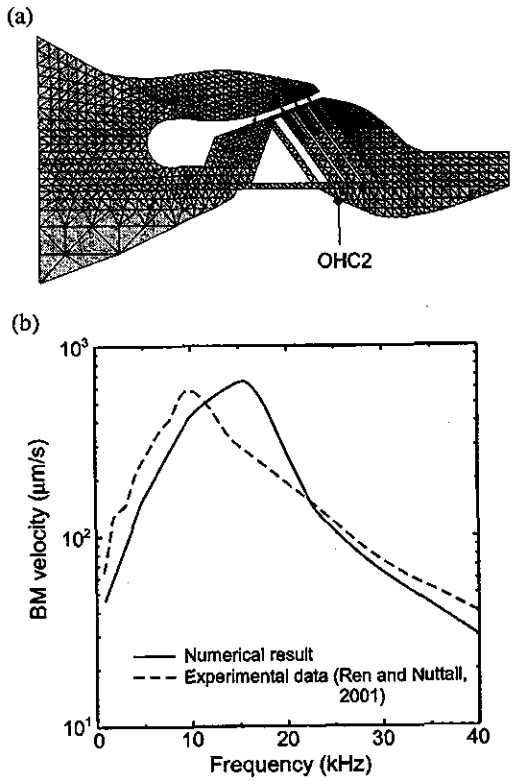

FIG. 9. Velocities of the basilar membrane when a pure tone of 80 dB SPL is applied to the ear canal. (a) Velocity measurement point on the BM. OHC2 is the abbreviation for the OHC of the second row. (b) Numerically obtained velocity of the BM and the experimental one (Ren and Nuttall, 2001) at the position which is indicated in (a). The CF of the model and best frequency of the experiment are 16 and 10 kHz, respectively.

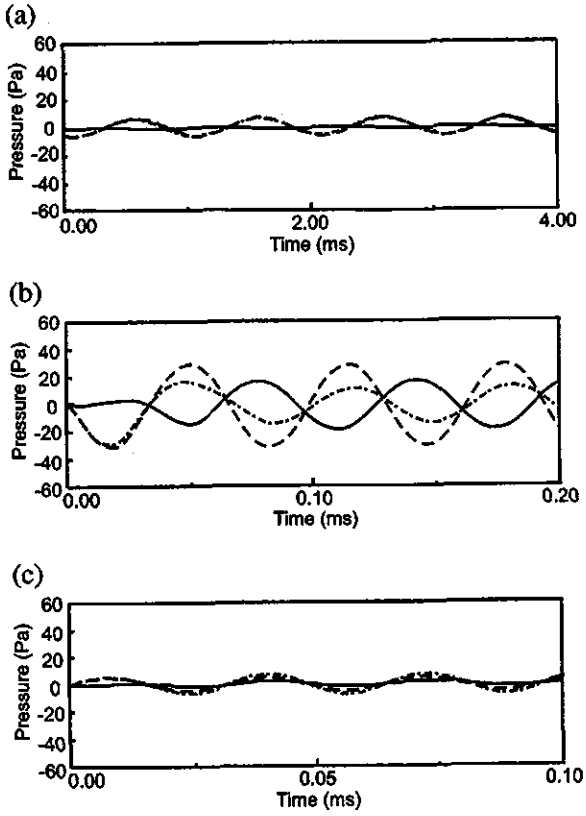

FIG. 10. Time courses of the pressure in the ST at 7 μm from the BM when pressure waves determined in Sec. IV are applied to the model. Three types of pressures are shown in each graph, i.e., the initial pressure which is a summation of the fast and slow waves (dashed line), the pressure caused by the vibration of the OC (solid line), and the resulting pressures including the fluid–structure interaction (dot–dashed line). (a) f=1 kHz. (b) f=16 kHz. (c) f=30 kHz.

sequently, it can be said that the magnitude and phase of the fast and slow waves are appropriately predicted for the most part.

V. VELOCITY OF THE BM AS A FUNCTION OF FREQUENCY

To confirm the validity of the model, the velocity of the BM obtained by the model is compared with that of the experimental data. Using a laser interferometer microscope, Ren and Nuttall (2001) measured the velocity the BM at the basal turn of the gerbil cochlea as a function of frequency. As the force generated by the OHC motility is not included in the model, the post-mortem BM velocity in their study is compared with the numerically obtained velocity of the BM. The best frequency, where the BM velocity takes a maximum, at the location of the measurement is approximately 10 kHz, although the CF of the model is 16 kHz. The distance between the location for the CF of 10 kHz and that of 16 kHz is approximately 7% of the entire length of the BM (Müller, 1996). Moreover, Allen and Sondhi (1979) calculated the frequency response of the velocity of the BM vibration at different locations along the BM, and showed nearly the same shapes of the frequency response at locations corresponding to the CF of 10 and 20 kHz. For these reasons, a comparison between the experimental data and the numerical result is acceptable.

The velocity of the BM is analyzed at the radial position of the second row of OHCs indicated in Fig. 9(a), where the laser beam is focused on the BM in the experiment. Figure 9(b) shows a comparison between the numerically obtained velocity of the BM and experimental one as a function of frequency. Although the frequency where the BM velocity has a maximum value is different, namely, 16 kHz in the model and 10 kHz in the measurement, the shape of the numerical result is similar to that of the experimental data. Therefore, the predicted pressure waves appear to be somewhat reliable. Moreover, it is found that although a pressure notch occurs at 18 kHz as shown in Fig. 7(b), there is no drastic change in the frequency response of the BM vibration.

VI. EFFECT OF THE FLUID–STRUCUTRE INTERACTION

To confirm the effect of the fluid–structure interaction in the model, the time courses of each pressure at 7 μm from the BM in the ST are depicted. In Fig. 10, the dashed line indicates the initial pressure which is a summation of the fast and slow waves, the solid line indicates the pressure caused by the vibration of the OC and the dot-dashed line indicates the resulting pressure including the F-S interaction, i.e., a summation of the two above-mentioned pressures.

At 16 kHz, which is the CF of the model, the pressure caused by the OC vibration is comparable to the initial pressure in magnitude (approximately 40%), and their phases are

opposite. Therefore, the resulting pressure is significantly influenced by the pressure caused by the OC vibration. On the other hand, at 1 and 30 kHz, which are well below or above the CF, the resulting pressure is nearly the same as the initial pressure because the pressure caused by the OC vibration is small relative to the initial pressure. The above-mentioned considerations ensure that the fluid–structure interaction considerably influences the response of the model at frequencies close to the CF. Moreover, by employing time course representation of the pressure in the ST, it is found that pressure fluctuation in the ST reaches a steady state within one cycle at 16 kHz. This is clearly shown in Fig. 10(b).

VII. CONCLUSIONS

A fluid–structure interaction model of the OC is constructed by coupling the two-dimensional OC model and three-dimensional fluid models, and unknown mechanical properties of the model are validated with the experimental results of trajectories within the OC in the hemicochlea. By comparison between numerical results and those of intracochlear pressure measurement, the magnitude and phase of the fast and slow waves are predicted. The frequency response of the BM is then simulated. Conclusions are as follows:

(1) When a pure tone of 80 dB SPL is applied to the ear canal, the magnitude of the fast wave in the SV, which is 105 dB SPL at 1 kHz, increases with increasing frequency and reaches 112 dB SPL at 40 kHz. The phase of the fast wave in the SV is 0° for the entire frequency range. The magnitude of the fast wave in the ST also increases with increasing frequency, but the magnitude in the ST is somewhat lower than that in the SV, i.e., 90 dB SPL at 1 kHz and 111 dB SPL at 40 kHz. The phase of the fast wave in the ST is 60° in the low frequency range and becomes 0° above the CF. The magnitude of the slow wave is the same as that of the fast wave in the SV at 1 kHz (105 dB SPL), and increases gradually with increasing frequency until it reaches a maximum of 125 dB SPL at the CF. It then falls sharply to 70 dB SPL. The phase of the slow wave starts at 0° and is significantly delayed near the CF and becomes −360° above the CF.

(2) It is found that although a pressure notch, which is caused by destructive interference between the fast wave and the slow wave in the ST, occurs in the ST pressure in the vicinity of the BM at 18 kHz, there is no drastic change in the frequency response of the BM vibration.

(3) The F-S interaction considerably influences the response of the OC at frequencies close to the CF.

(4) The pressure fluctuation in the ST seems to reach a steady state within one cycle.

ACKNOWLEDGMENTS

The authors thank Elizabeth S. Olson and Claus-Peter Richter for their comments which were useful in improving the model. This work was supported by a grant from the Human Frontier Science Program, by a Health and Labor Science Research Grant from the Ministry of Health, Labor and Welfare of Japan, by Grant-in-Aid for Scientific Research (B) (2) 13557142 and Grant-in-Aid for Scientific Research on Priority Areas 15086202 from the Ministry of Education, Culture, Sports, Science and Technology of Japan, and by the 21st Century COE Program Special Research Grant of the "Future Medical Engineering Based on Bionanotechnology."

Allen, J. B., and Sondhi, M. M. (**1979**). "Cochlear Macromechanics Time Domain Solutions," J. Acoust. Soc. Am. **66**, 123–132.

Ashman, R. B., Cowin, S. C., Van Buskirk, W. C., and Rice, J. C. (**1984**). "A continuous wave technique for the measurement of the elastic properties of cortical bone," J. Biomech. **17**, 349–361.

Edge, R. M., Evans, B. N., Pearce, M., Richter, C.-P., Hu, X., and Dallos, P. (**1998**). "Morphology of the unfixed cochlea," Hear. Res. **124**, 1–16.

Harlow, F. H., and Welch, J. E. (**1965**). "Numerical calculation of time-dependent viscous incompressible flow of fluid with free surface," Phys. Fluids **8**, 2182–2189.

Hu, X., Evans, B. N., and Dallos, P. (**1999**). "Direct visualization of organ of Corti kinematics in a hemicochlea," J. Neurophysiol. **82**, 2798–2807.

Kolston, P. J., and Ashmore, J. F. (**1996**). "Finite element micromechanical modeling of the cochlea in three dimensions," J. Acoust. Soc. Am. **99**, 455–467.

Laffon, E., and Angelini, E. (**1996**). "On the Deiters cell contribution to the micromechanics of the organ of Corti," Hear. Res. **99**, 106–109.

Langer, M. G., Fink, S., Koitschev, A., Rexhausen, U., Hober, J. K. H., and Ruppersberg, J. P. (**2001**). "Lateral mechanical coupling of stereocilia in cochlear hair bundles," Biophys. J. **80**, 2608–2621.

Lighthill, J. (**1981**). "Energy flow in the cochlea," J. Fluid Mech. **106**, 149–213.

Müller, M. (**1996**). "The cochlear place-frequency map of the adult and developing mongolian gerbil," Hear. Res. **94**, 148–156.

Naidu, R. C., and Mountain, D. C. (**1998**). "Measurements of the stiffness map challenge a basic tenet of cochlear theories," Hear. Res. **124**, 124–131.

Newmark, N. M. (**1959**). "A method of computation for structural dynamics," J. Eng. Mech. Div. **85**, 67–94.

Olson, E. S. (**1999**). "Direct measurement of intra-cochlear pressure waves," Nature (London) **402**, 526–529.

Olson, E. S. (**2001**). "Intracochlear pressure measurements related to cochlear tuning," J. Acoust. Soc. Am. **110**, 349–367.

Ren, T. (**2002**). "Longitudinal pattern of basilar membrane vibration in the sensitive cochlea," Proc. Natl. Acad. Sci. U.S.A. **99**, 17101–17106.

Ren, T., and Nuttall, A. L. (**2001**). "Basilar membrane vibration in the basal turn of the sensitive gerbil cochlea," Hear. Res. **151**, 48–60.

Steele, C. R., Baker, G., Tolomeo, J., and Zetes, D. (**2000**). "Cochlear Mechanics," in *The Biomedical Engineering Handbook*, 2nd ed., edited by J. D. Bronzino (CRC Press, Boca Raton, FL), pp. 1–12.

Tolomeo, J. A., and Holley, M. C. (**1997**). "Mechanics of microtubule bundles in pillar cells from the inner ear," Biophys. J. **73**, 2241–2247.

Ulfendahl, M., and Chen, E. (**1998**). "Axial and transverse stiffness measures of cochlear outer hair cells suggest a common mechanical basis," Pfluegers Arch. **436**, 9–15.

Zetes, D. E., and Steele, C. R. (**1997**). "Fluid–structure interaction of the stereocilia bundle in relation to mechanotransduction," J. Acoust. Soc. Am. **101**, 3593–3601.

Available online at www.sciencedirect.com
SCIENCE DIRECT
Hearing Research 192 (2004) 57–64
HEARING RESEARCH
www.elsevier.com/locate/heares

Mechanical properties of sensory and supporting cells in the organ of Corti of the guinea pig cochlea – study by atomic force microscopy

Michiko Sugawara, Yuya Ishida, Hiroshi Wada *

Department of Bioengineering and Robotics, Tohoku University, Aoba-yama 01, Sendai 980-8579, Japan

Received 30 June 2003; accepted 20 January 2004
Available online 5 March 2004

Abstract

Mammalian hearing is refined by amplification of the motion of the cochlear partition. To understand the cochlear amplification, mechanical models of the cochlea have been used. When the dynamic behavior of the cochlea is analyzed by a model, elastic properties of the cells in the organ of Corti must be determined in advance. Recently, elastic properties of outer hair cells (OHCs) and pillar cells have been elucidated. However, those of other cells have not yet been clarified. Therefore, in this study, using an atomic force microscope (AFM), elastic properties of Hensen's cells, Deiters' cells and inner hair cells (IHCs) in the apical turn and those in the basal and second turns were estimated. As a result, slopes indicative of cell elastic properties were $(8.9 \pm 5.8) \times 10^3$ m^{-1} for Hensen's cells ($n = 30$), $(5.5 \pm 5.3) \times 10^3$ m^{-1} for Deiters' cells ($n = 20$) and $(3.8 \pm 2.6) \times 10^3$ m^{-1} for IHCs ($n = 20$), and Young's modulus were 0.69 ± 0.45 kPa for Hensen's cells and 0.29 ± 0.20 kPa for IHCs. There was no significant difference between elastic properties of each type of cell in the apical turn and those in the basal and second turns. However, it was found that there is a significant difference between Young's moduli of cells estimated in this study and those of the OHCs and pillar cells reported previously.

Keywords: Hensen's cells; Deiters' cells; Inner hair cells; Mechanical properties; Atomic force microscopy

1. Introduction

The mammalian ear has is characterize by sensitivity, broad dynamic range and sharp tuning. These characteristics are based on cochlear amplification, which is believed to be dependent on the voltage-dependent electromotile response of the outer hair cells (OHCs) in the organ of Corti (Brownell et al., 1985; Kachar et al., 1986). To understand cochlear amplification fully, it is necessary to characterize the role played by the involved components, namely, the basilar membrane, tectorial membrane and the organ of Corti containing OHCs, inner hair cells (IHCs), Deiters' cells, Hensen's cells, pillar cells and so on. For that purpose, mechanical models of the cochlea have been developed and evaluated (Kolston and Ashmore, 1996; Kolston, 1999; Steele, 1999; Bonke and Arnold, 1999), because direct observation of mechanical motion within the organ of Corti in vivo is currently difficult due to the extreme vulnerability of the cochlear amplifier to surgical insult. However, most of the mechanical properties of the cells in the organ of Corti have not yet been clarified. Therefore, to understand the cochlea mechanics, the mechanical properties of the cells in the organ of Corti should be determined in advance.

Tolomeo and Holley (1997) conducted a study of elastic properties in isolated guinea pig outer pillar cells. Using a three-point bending test, Young's modulus of pillar cells was determined to be 2×10^6 kPa. Pillar cells possess a cytoskeleton composed of thousands of

* Corresponding author. Tel.: +81-22-217-6938; fax: +81-22-217-6939.
E-mail address: wada@cc.mech.tohoku.ac.jp (H. Wada).
Abbreviations: IHC, inner hair cell; OHC, outer hair cell; AFM, atomic force microscopy

0378-5955/$ - see front matter © 2004 Elsevier B.V. All rights reserved.
doi:10.1016/j.heares.2004.01.014

parallel, cross-linked microtubules and actin filaments. It is known that the mechanical properties of cells are regulated by the structure of the cytoskeleton of the cells. Recently, using the contact mode of an atomic force microscope (AFM), Sugawara et al. (2002) reported that Young's modulus of the OHCs in the apical turn was 2.0 ± 0.81 kPa, whereas that of the OHCs in the basal and second turns was 3.7 ± 0.96 kPa. The difference in Young's modulus of the OHCs in each turn of the cochlea might affect the dynamic behavior of the organ of Corti. However, elastic properties of other cells in the organ of Corti have not yet been clarified. Therefore, in this study, an attempt was made to estimate elastic properties of Hensen's cells, Deiters' cells and IHCs in the apical turn and those in the basal and second turns with an AFM.

2. Materials and methods

2.1. Cell preparation

Eighty-eight ears of guinea pigs weighing between 200 and 500 g were used. After the bulla had been opened, the cochlea was detached and transferred to an experimental bath (the major ions in the medium were NaCl, 140 mM; KCl, 5 mM; $CaCl_2$, 1.5 mM; $MgCl_2 \cdot 6H_2O$, 1.5 mM; HEPES, 5 mM; Glucose, 5 mM; pH 7.2; 300 mOsm). The bony shell covering the cochlea was removed and the apical, second and basal turns of the organ of Corti were gently scraped off from the basilar membrane, and Hensen's cells and Deiters' cells were isolated by gently pipetting the organ of Corti in the experimental bath. In the case of the isolation of IHCs, the organ of Corti was transferred to an enzymatic digestion medium which contained 1 ml of the experimental bath medium and 1 mg trypsin. After enzymatic incubation for 15 min, IHCs were isolated by gently pipetting the organ of Corti in the experimental bath. By means of these isolation procedures, cells from the apical turn and those from the basal and second turns were identified. All experiments were performed at room temperature. The care and use of the animals in this study were approved by the Institutional Animal Care and Use Committee of Tohoku University, Sendai, Japan.

2.2. Atomic force microscopy

AFM is a valuable tool for evaluating elastic properties under physiological conditions (Radmacher, 1997). In this study, in order to evaluate elastic properties of cells in the organ of Corti, AFM studies were performed with a commercial instrument (NVB100, Olympus), in which the AFM unit is mounted on an inverted microscope. A v-shaped silicon nitride cantilever (OMCL-TR400PSA-2, Olympus) with a spring constant of 0.02 N/m was used. The typical radius of curvature of the cantilever tip was less than 20 nm.

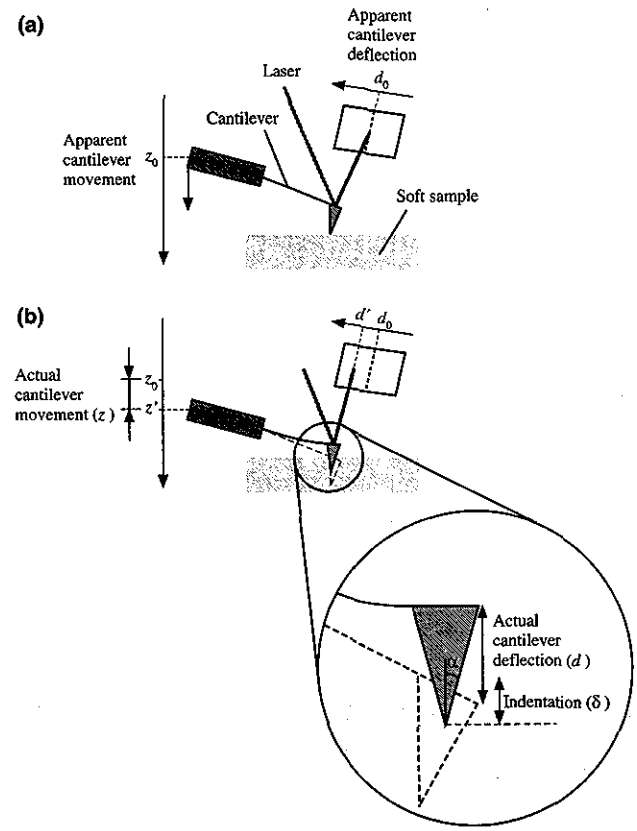

Fig. 1. Schematic of the cantilever on a soft sample. (a) Contact point – When the tip of the cantilever touches a sample, the apparent cantilever movement and the apparent cantilever deflection are defined as (z_0) and (d_0), respectively. (b) Indentation of the cell. When the cantilever is deflected, the actual deflection of the cantilever (d) is equal to ($d' - d_0$), where d' is the apparent cantilever deflection. Both (d') and (d_0) are detected by an optical detector which consists of a laser, a mirror and a photodiode array. At this stage, the actual movement of the cantilever (z) is equal to ($z' - z_0$), where (z') is the apparent cantilever movement. Indentation of the sample (δ) is given by $\delta = z - d$.

When the cantilever is moved by the piezoelectric scanner and the tip comes in contact with a sample, the cantilever is deflected (Fig. 1). The deflection of the cantilever is detected by an optical detector, in which a laser beam focused on the cantilever is reflected toward a photodiode array which acts as a position detector. Using this AFM system, a force curve which represents the relationship between the apparent cantilever deflection (d') and the apparent cantilever movement (z') caused by the piezoelectric scanner is obtained.

2.3. Analysis of the force curves

An example of the relationship between the apparent cantilever deflection (d') and the apparent cantilever

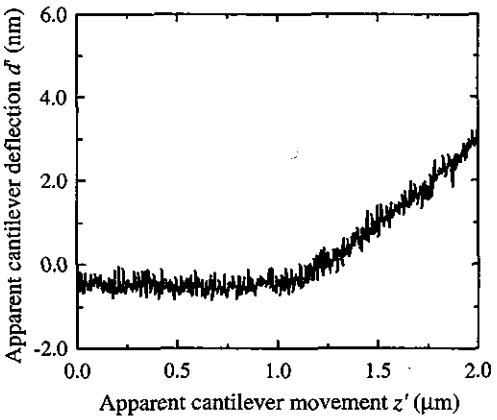

Fig. 2. Relationship between the apparent cantilever deflection (d') and the apparent cantilever movement (z') on the Hensen's cell.

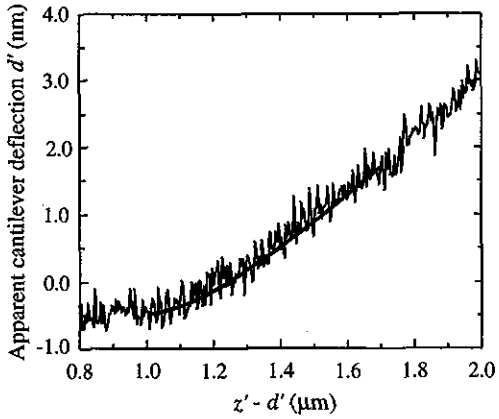

Fig. 3. Relationship between the apparent cantilever deflection (d') and the difference between the apparent cantilever deflection and the apparent cantilever movement ($z' - d'$) obtained from Fig. 2. By fitting this figure with Eq. (5) by the least squares method, the slope (a) is obtained. In addition, by comparing the slope (a) with $2E\tan\alpha/\pi k(1-\nu^2)$, Young's modulus is determined. Thin and thick lines represent the measurement data and the square regression line, respectively. In the analysis, Poisson's ratio was assumed to be 0.499, the half-opening angle and spring constant of the cantilever were 17° and 0.02 N/m, respectively, and Young's modulus was determined to be 0.26 kPa.

movement (z') on the Hensen's cell obtained from the AFM is shown in Fig. 2. Assuming that the contact point is (z_0, d_0) (Fig. 1(a)), the actual cantilever deflection (d) and the actual cantilever movement (z) can be written as follows:

$$d = d' - d_0, \tag{1}$$

$$z = z' - z_0. \tag{2}$$

As the difference between the actual cantilever movement (z) and the actual cantilever deflection (d) represents the sample indentation (δ) the indentation is given by

$$\delta = z - d, \tag{3}$$

which is shown in Fig. 1(b).

Several methods have been proposed to obtain the relationship between the cantilever deflection (d) and the sample indentation (δ). Sugawara et al. (2002) visually truncated the contact point and obtained the relationship between them. They then estimated the elastic properties of the sample by fitting the square regression line to this relationship. Some other researchers (Radmacher et al., 1996; Dimitriadis et al., 2002) proposed a method to determine the contact point together with the elastic properties of the sample numerically. As our previous method may possibly include some errors in determining the contact point, which could lead to incorrect elastic properties, in this study, an attempt was made to numerically determine the contact point together with the elastic properties.

Substituting Eqs. (1) and (2) into Eq. (3), the indentation is given by

$$\delta = z - d = (z' - d') - (z_0 - d_0). \tag{4}$$

From Fig. 2, the relationship between the apparent cantilever deflection (d') and the difference between the apparent cantilever deflection and the apparent cantilever movement ($z' - d'$) is obtained and shown in Fig. 3. It was possible to fit the curve in this figure with a square regression line given by

$$d' = a\{(z' - d') - b\}^2 + c, \tag{5}$$

and the parameters (a), (b) and (c) were obtained by the least squares method.

The parameter (a) is a representative of the elastic properties of the sample. When the tip of the cantilever comes in contact with a sample, the cantilever is deflected. If the sample is harder, the sample indentation is smaller and the cantilever deflection is larger, which leads to a larger slope in Fig. 1 and also in Fig. 2.

When the sample is elastic, isotropic and homogeneous and the tip is rigid and conical, the Hertz model, which describes the elastic response of a sample indented by the tip of the cantilever, is applied to the measurement data. When the tip is conical with a half opening angle (α), the relationship between the actual cantilever deflection (d) and the actual indentation (δ) is given by

$$d = \{2E\tan\alpha/\pi k(1-\nu^2)\}\delta^2, \tag{6}$$

where (k), (E) and (ν) represent the spring constant of the cantilever, Young's modulus of the sample and Poisson's ratio of the sample, respectively (Snedon, 1965; Wu et al., 1998). The substitution of Eqs. (2) and (4) into Eq. (6) results in the following equation:

$$d' = \{2E\tan\alpha/\pi k(1-\nu)^2\}\{(z' - d') - (z_0 - d_0)\}^2 + d_0. \tag{7}$$

The half-opening angle and the spring constant of the cantilever used in this experiment were 17° and 0.02 N/

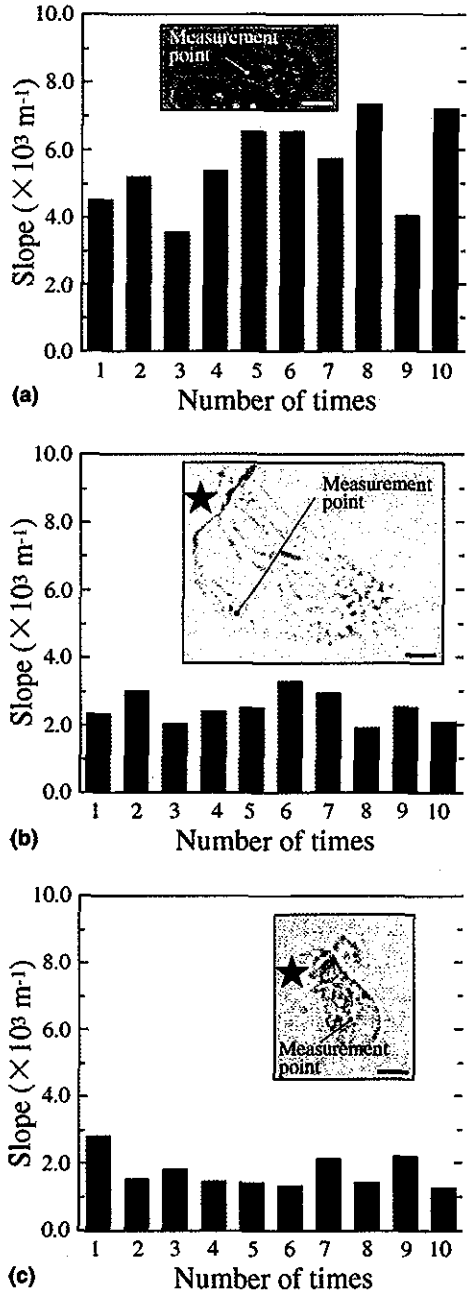

Fig. 4. The slopes calculated from the curves measured at the middle part of the cell. In this measurement, as the relationship between (d') and ($z' - d'$), which is shown in Fig. 3, was obtained 10 times at one point, the slope was calculated by fitting the relationship with a square regression line by the least squares method. (a) Hensen's cell – The mean slope is $(5.6 \pm 1.3) \times 10^3$ m^{-1} ($n = 10$). (b) Deiters' cell – The mean slope is $(2.5 \pm 0.44) \times 10^3$ m^{-1} ($n = 10$). (c) IHC – The mean slope is $(1.7 \pm 0.49) \times 10^3$ m^{-1} ($n = 10$). In each figure, an inset represents the measurement point on the cell. Bar = 10 μm. In (b) and (c), the star mark represents the side of the reticular lamina.

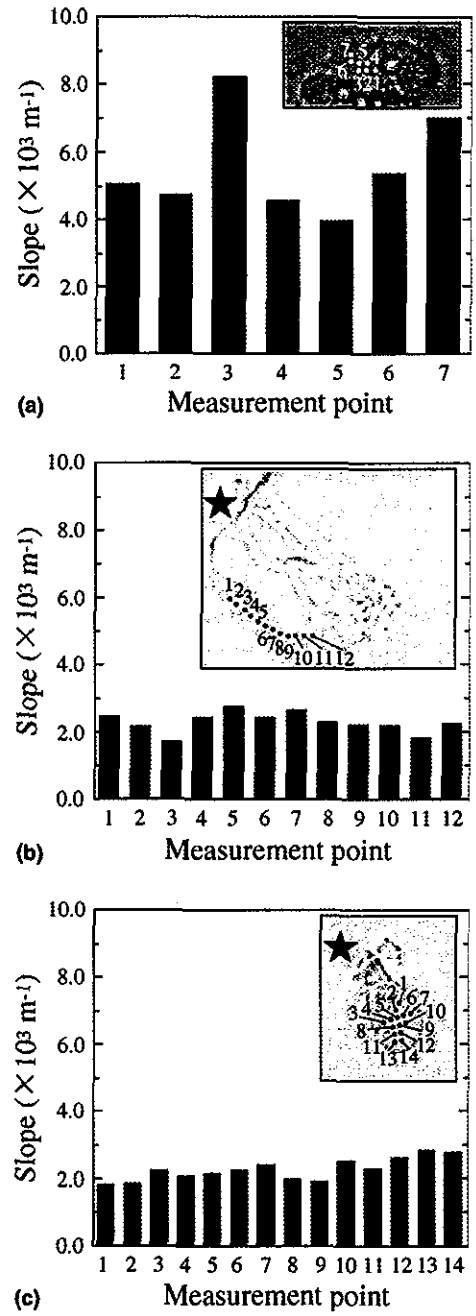

Fig. 5. The slopes calculated from the curves measured at several points on the cell. At each measurement point, the relationship between (d') and ($z' - d'$) was obtained five times, and the five slopes calculated from the relationships were averaged. (a) Hensen's cell – The mean slope is $(5.6 \pm 1.5) \times 10^3$ m^{-1}. (b) Deiters' cell – The mean slope is $(2.3 \pm 0.30) \times 10^3$ m^{-1}. (c) IHC – The mean slope is $(2.2 \pm 0.33) \times 10^3$ m^{-1}. In each figure, an inset represents measurement points on the cell, and the numbers in the inset correspond to those shown on the horizontal axis of the figure. In (b) and (c), the star mark represents the side of the reticular lamina.

m, respectively, and Poisson's ratio was assumed to be 0.499 since samples were biomaterials. When the Hertz model is applied to the analysis of the curve, as the slope (a) is equivalent to $2E \tan\alpha/\pi k(1 - \nu^2)$, with the parameters α, k and ν being given, Young's modulus (E) of the sample is estimated from this relationship. In addition, as the parameters (b) and (c) correspond to $(z_0 - d_0)$ and (d_0), respectively, the contact point (z_0, d_0) is also determined.

2.4. Variance of slopes in the measurement

In this study, the noise in the recorded force curve caused variance of the slopes. Therefore, first, such variance was evaluated by obtaining the relationship between (d') and ($z' - d'$) 10 times at one point in the middle region of each cell and calculating the mean and standard deviation of the slope. The elastic properties of the nucleus might be greater than the other components of the cell's cytoplasm. Therefore, to avoid data scattering, measurements on the nuclei of Hensen's cells, Deiters' cells and IHCs were avoided. The results are shown in Fig. 4. Next, variance of the slopes caused by the differences in the locations of the measurement points was evaluated. At each measurement point, the relationship between (d') and ($z' - d'$) was obtained five times, and the five slopes calculated from the relationships were averaged. The results are shown in Fig. 5. In the measurement of OHCs, Sugawara et al. (2002) reported that the mean and standard deviation of the slope measured 10 times at one point in the middle region of an OHC and that measured at 21 points at intervals of 10 nm in the circumferential direction in the middle region of an OHC are $(7.6 \pm 0.37) \times 10^3$ m^{-1} ($n = 10$) and $(6.8 \pm 0.73) \times 10^3$ m^{-1} ($n = 10$), respectively. The latter variance is larger than the former one, which means that the slope obtained for an OHC depends on the location. On the other hand, comparison between Figs. 4 and 5 shows that the variance of the slopes due to the difference in the location of the measurement point in each cell is almost the same as that caused by the measurement 10 times at one point, i.e., the slope obtained for each cell is not dependent on the location of the measurement point. Therefore, to reduce the measurement time in this experiment, five force curves were obtained at one point, and the mean and standard deviation of the slopes were calculated for each cell.

3. Results

First, the relationships between the cantilever deflection and the indentation of Hensen's cells in the apical turn and those in the basal or second turns were measured. In this measurement, these relationships were not obtained for lipid droplets nor the nucleus in the cytoplasm, because the Hertz model is based on the assumption of the homogeneity of the sample. The fitting of square regression lines to the relationships between the cantilever deflection and the indentation of Hensen's cells led to estimates of the parameter a. The value obtained from the apical turn and that obtained in the basal turn or second turn were $(11.1 \pm 6.5) \times 10^3$ m^{-1} ($n = 15$) and $(6.8 \pm 4.2) \times 10^3$ m^{-1} ($n = 15$), respectively. There was no significant difference between the slope of Hensen's cells in the apical turn and that in the basal turn or second turn (Mann–Whitney test; $P < 0.05$), and the average of the slopes of the Hensen's cells in the basal, second and apical turns was $(8.9 \pm 5.8) \times 10^3$ m^{-1} ($n = 30$) (Table 1).

Next, the slopes of the Deiters' cells in the apical turn and those in the basal turn or second turn were estimated. In this measurement, the force curves of the Deiters' cells were obtained in the middle region, because that region is not on the nucleus nor on the phalangeal process which cannot be regarded as flat. The slope obtained from Deiters' cells in the apical turn and that in the basal turn or second turn were $(3.6 \pm 2.5) \times 10^3$ m^{-1} ($n = 10$) and $(7.3 \pm 6.7) \times 10^3$ m^{-1} ($n = 10$), respectively. There was no significant difference between the slope of Deiters' cells in the apical turn and that in the basal turn or second turn (Mann–Whitney test; $P < 0.05$), and the average of the slopes of the Deiters' cells in the basal, second and apical turns was $(5.5 \pm 5.3) \times 10^3$ m^{-1} ($n = 20$) (Table 1).

Finally, the slopes of the IHCs in the apical turn and those in the basal and second turns were estimated. In this measurement, ideally, the effect of trypsin on cells should have been evaluated before it was used for the isolation of the IHCs. However, as it was difficult to isolate IHCs without trypsin, this was not possible. On the other hand, OHCs can be isolated without trypsin. In addition, as OHCs have cytoskeletons which maintain the cell shape in vitro, it is considered that the effect of trypsin can be evaluated by examining the length change of the OHCs. Therefore, OHCs were incubated in an enzymatic digestion medium which contained 1 ml experimental bath medium and 1 mg trypsin for 30 min, and the length change of the OHCs during such incubation was measured. As a result, the mean value of the cell length after enzymatic incubation was found to be $98.4 \pm 1.4\%$ ($n = 10$), which was obtained by dividing the resulting cell length by the initial length. In addition, it is presumed that trypsin, which has a molecular weight of 23,300, cannot pass through the cell membrane. Therefore, its effect on the structure of IHCs might be negligible. In the measurement of the IHCs, as with the Hensen's cells and Deiters' cells, the force curves of the IHCs were obtained in the middle region, which is not on the nucleus. The slope obtained from the curve measured on IHCs in the apical turn and that in the basal turn or second turn were $(4.1 \pm 3.2) \times 10^3$ m^{-1}

Table 1
Slopes obtained on the cells in the organ of Corti

Cell	Slope ($\times 10^3$ m^{-1})	Number
Hensen's cell	8.9 ± 5.8	30
Deiters' cell	5.5 ± 5.3	20
IHC	3.8 ± 2.6	20

($n = 10$) and $(3.4 \pm 1.8) \times 10^3$ m^{-1} ($n = 10$), respectively. There was no significant difference between the slope of IHCs in the apical turn and that in the basal turn or second turn (Mann–Whitney test; $P < 0.05$), and the average of the slopes of the IHCs in the basal, second and apical turns was $(3.8 \pm 2.6) \times 10^3$ m^{-1} ($n = 20$) (Table 1).

4. Discussion

4.1. Young's modulus of cells

Using the AFM, the slopes of Hensen's cells, Deiters' cells and IHCs were estimated under physiological conditions. When the sample is elastic, isotropic and homogeneous, the Hertz model accurately describes the deflections measured in the AFM method, and Young's modulus may be estimated from the measured slopes. In the case of OHCs, when the cell's mechanical properties were evaluated by the AFM, both the orthotropic lateral wall and the isotropic cytoplasm were indented by the cantilever. As the thickness of the lateral wall is only 100 nm and the cytoplasm is much thicker than the lateral wall, the OHC can be assumed to be isotropic. However, in Deiters' cells, Slepecky and Chamberlain (1983, 1987) showed that microtubules run axially from the base of the cell close to the basilar membrane up to the reticular lamina. They also demonstrated that these microtubules exist not only at the lateral wall of the cell but also inside the cell. Therefore, it is presumed that Deiters' cells are anisotropic, and thus the Hertz model was not applied to the slopes of these cells. On the other hand, as both Hensen's cells and IHCs have no such structures as those seen in Deiters' cells, it is estimated that Hensen's cells and IHCs are isotropic. Therefore, Young's moduli were calculated from their slopes in Hensen's cells and IHCs, and were determined to be 0.69 ± 0.45 and 0.29 ± 0.20 kPa, respectively. They are shown in Table 2, together with the previously reported Young's moduli of the OHCs and pillar cells.

Young's moduli of various types of cells shown in Table 2 could be worthy of consideration. Firstly, comparison of Young's modulus of OHCs with those of Hensen's cells and IHCs shows that the former is larger than the latter, which suggests that the stiffness of OHCs is also greater. As the stiffness is directly related to the force produced by OHCs, i.e., the larger the stiffness, the larger the force, it is expected that OHCs are suitable for producing force in the organ of Corti. Secondly, comparison of Young's modulus of pillar cells with those of others shows that it is six orders of magnitude larger than any other cell type in Table 2. This result implies that the pillar cell can be considered to be a rigid structure when constructing a cochlear model.

4.2. Relationship between Young's modulus and the cell structure

Comparison of Young's moduli of Hensen's cells and IHCs obtained in this study with Young's modulus of OHCs reveals a significant difference (Mann–Whitney test; $P < 0.05$). In addition, Young's moduli of the cells obtained in this study were much smaller than that of the pillar cells (Table 2). From the evidence that the difference in elastic properties of the OHC in various parts of the cell is due to the difference in the cell structure, especially the difference in the number of filaments in the cell (Wada et al., 2003), one of the reasons for the difference in Young's moduli might be due to the difference in the cell structure. The OHC lateral wall consists of the plasma membrane, cortical lattice and subsurface cisternae (Holley and Ashmore, 1988). From immunological studies, the cortical lattice has been shown to be composed of a dense network of circumferential actin filaments and cross-linked spectrin (Holley and Ashmore, 1990; Holley et al., 1992; Nishida et al., 1993). These filaments are considered to be related to the elastic properties of the OHC. Pillar cells possess a cytoskeleton composed of thousands of parallel, cross-linked microtubules and actin filaments. Therefore, it is expected that these cells have a rigid structure. On the other hand, it has been confirmed that Hensen's cells consist of actin filaments and spectrin under the lipid bilayer (Slepecky et al., 1990; Mahendrasingam et al., 1998), and IHCs are known to consist of actin filaments, spectrin and microtubules under the lipid bilayer (Slepecky and Ulfendahl, 1992; Mahendrasingam et al., 1998). However, a cytoskeletal network as seen in the lateral wall of the OHC or in the pillar cell has not been confirmed in Hensen's cells and IHCs. Therefore, it is considered that the differ-

Table 2
Young's modulus of the cells in the organ of Corti

Cell	Young's modulus (kPa)	Number	References
Hensen's cell	0.69 ± 0.45	30	This study
IHC	0.29 ± 0.20	20	This study
OHC (in the apical turn)	2.0 ± 0.81	20	Sugawara et al. (2002)
OHC (in the basal and second turns)	3.7 ± 0.96	20	Sugawara et al. (2002)
Pillar cell	2×10^6		Tolomeo and Holley (1997)

ence between Young's moduli of Hensen's cells and those of IHCs obtained in this study and those of OHCs and pillar cells reported previously is due to the difference in the cell structure.

4.3. Difference in Young's modulus of the cell in each turn of the cochlea

Sugawara et al. (2002) reported that there is a significant difference between Young's moduli of the OHCs in the apical turn and that in the basal or second turns. As OHCs are constituents of the organ of Corti, a difference in the elastic properties of OHCs might affect the dynamic behavior of the organ of Corti along the length of the cochlea. As well as in the OHCs, significant differences between Young's modulus of Hensen's cells or IHCs in the apical turn and that in the basal or second turns were expected. However, no such significant differences were found. Taking only Young's modulus into consideration, this result implies that none of these cells affect the dynamic behavior of the organ of Corti along the length of the cochlea. However, there is another factor that has an effect on its dynamic behavior, that is, the shape of each cell which changes its mass.

It is known that there is a difference in the shape of Hensen's cells from turn to turn. The cells increase in size toward the apical turn (Santi, 1988). Such a difference in shape causes a difference in the mass of the cell. Therefore, it is suggested that variation in the local shape of the Hensen's cell is responsible, in part, for the variation in the dynamic behavior of the organ of Corti along the length of the cochlea. By contrast, the height of the cell body of the IHC, which has the shape of a flask with a diameter of about 9–13 μm at the widest point and a length of 20–25 μm (David et al., 2001), is fairly constant over the extent of the entire cochlea. Therefore, it is expected that the IHCs do not affect the dynamic behavior of the organ of Corti along the length of the cochlea.

5. Conclusions

In this study, the elastic properties of Hensen's cells, Deiters' cells and IHCs were estimated with an AFM. The results are as follows:

1. The slopes, which correspond to the elastic properties, of Hensen's cells, Deiters' cells and IHCs were $(8.9 \pm 5.8) \times 10^3$, $(5.5 \pm 5.3) \times 10^3$ and $(3.8 \pm 2.6) \times 10^3$ m^{-1}, respectively. There was no significant difference between elastic properties of the cells in the apical turn and those in the basal and second turns.
2. Young's moduli of Hensen's cells and IHCs were 0.69 ± 0.45 and 0.29 ± 0.20 kPa, respectively.
3. It was suggested that the difference between Young's moduli of the cells estimated in this study and those of OHCs and pillar cells reported previously is due to the difference in the cell structure.

Acknowledgements

The authors wish to thank Mr. A. Yagi, Olympus Optical Co., Ltd. and Mr. E. Imai, Olympus Promarketing, Inc., for technical assistance. This work was supported by a grant from the Human Frontier Science Program, by a grant from the Foundation Advanced Technology Institute, by a Health and Labour Science Research Grant from the Ministry of Health, Labour and Welfare of Japan, and by a Grant-in-Aid for Scientific Research (A) 11307033, a Grant-in-Aid for Scientific Research for Young Scientists (B) 13770947 and a Grant-in-Aid for Scientific Research on Priority Areas 15086202 from the Ministry of Education, Culture, Sports, Science and Technology of Japan.

References

Bonke, F., Arnold, W., 1999. 3D-finite element model of the human cochlea including fluid-structure couplings. ORL 61, 305–310.

Brownell, W.E., Bader, C.R., Bertrand, D., de Ribaupierre, Y., 1985. Evoked mechanical responses of isolated cochlear outer hair cells. Science 227, 194–196.

David, Z.Z.H., Zheng, J., Edge, R., Dallos, P., 2000. Isolation of cochlear inner hair cells. Hear. Res. 145, 156–160.

Dimitriadis, E.K., Horkay, F., Maresca, J., Kachar, B., Chadwick, R.S., 2002. Determination of elastic moduli of thin layers of soft material using the atomic force microscope. Biophys. J. 82, 2798–2810.

Holley, M.C., Ashmore, J.F., 1988. A cytoskeletal spring in cochlear outer hair cells. Nature 335, 635–637.

Holley, M.C., Ashmore, J.F., 1990. Spectrin, actin and the structure of the cortical lattice in mammalian cochlear outer hair cells. J. Cell Sci. 96, 283–291.

Holley, M.C., Kalinec, F., Kachar, B., 1992. Structure of the cortical cytoskeleton in mammalian outer hair cells. J. Cell Sci. 102, 569–580.

Kachar, B., Brownell, W.E., Altschuler, R., Fex, J., 1986. Electrokinetic shape changes of cochlear outer hair cells. Nature 322, 365–368.

Kolston, P.J., 1999. Comparing *in vitro*, *in situ*, and *in vivo* experimental data in a three-dimensional model of mammalian cochlear mechanics. Proc. Natl. Acad. Sci. USA 96, 3676–3681.

Kolston, P.J., Ashmore, J.F., 1996. Finite element micromechanical modeling of the cochlea in three dimensions. J. Acoust. Soc. Am. 99, 455–467.

Mahendrasingam, S., Furness, D.N., Hackney, C.M., 1998. Ultrastructural localisation of spectrin in sensory and supporting cells of guinea-pig organ of Corti. Hear. Res., 151–160.

Nishida, Y., Fujimoto, T., Takagi, A., Honjo, I., Ogawa, K., 1993. Fodrin is a constituent of the cortical lattice in outer hair cells of the guinea pig cochlea: Immunocytochemical evidence. Hear. Res. 65, 274–280.

Radmacher, M., 1997. Measuring the elastic properties of biological samples with the AFM. IEEE Eng. Med. Biol. Mag. 16, 47–57.

Radmacher, M., Fritz, M., Kacher, C.M., Cleveland, J.P., Hansma, P.K., 1996. Measuring the viscoelastic properties of human platelets with the atomic force microscope. Biophys. J. 70, 556–567.

Santi, P.A., 1988. Cochlear microanatomy and ultrastructure. In: Jahn, A., Santos-Sacchi, F. (Eds.), Physiology of the Ear. Raven Press, New York, pp. 173–199.

Slepecky, N., Chamberlain, S.C., 1983. Distribution and polarity of actin in inner ear supporting cells. Hear. Res. 10, 359–370.

Slepecky, N., Chamberlain, S.C., 1987. Tropomyosin co-localizes with actin microfimaments and microtubules within supporting cells of the inner ear. Cell Tissue Res. 248, 63–66.

Slepecky, N.B., Ulfendahl, M., 1992. Actin binding and microtubule-associated proteins in the organ of Corti. Hear. Res. 57, 201–215.

Snedon, I.E., 1965. The relation between load and penetration in the axisymmetric boussinesq problem for a punch of arbitrary profile. Int. J. Eng. Sci. 3, 47–57.

Steele, C.R., 1999. Toward three-dimensional analysis of cochlear structure. ORL 61, 238–251.

Sugawara, M., Ishida, Y., Wada, H., 2002. Local mechanical properties of guinea pig outer hair cells measured by atomic force microscopy. Hear. Res. 174, 222–229.

Tolomeo, J.A., Holley, M.C., 1997. Mechanics of microtubule bundles in pillar cells from the inner ear. Biophys. J. 73, 2241–2247.

Wada, H., Usukura, H., Sugawara, M., Katori, Y., Kakehata, S., Ikeda, K., Kobayashi, T., 2003. Relationship between the local stiffness of the outer hair cell along the cell axis and its ultrastructure observed by atomic force microscopy. Hear. Res. 177, 61–70.

Wu, H.W., Kuhn, T., Moy, V.T., 1998. Mechanical properties of L929 cells measured by atomic force microscopy: Effects of anticytoskeletal drugs and membrane crosslinking. Scanning 20, 389–397.